

# Contents

<b>1</b>	<b>Neutral MSSM Higgs Bosons Search...</b>	<b>3</b>
1.1	Introduction . . . . .	4
1.2	Signal and Background Processes . . . . .	5
1.3	Analysis Strategy . . . . .	6
1.3.1	Simulated Event Samples . . . . .	7
1.4	Event Selections and Categorization . . . . .	8
1.4.1	Mass Reconstruction with MMC Technique . . . . .	10
1.5	Background Modeling and Validation . . . . .	12
1.5.1	Top Quark Pair Production Validation . . . . .	12
1.5.2	Multi-jet Background . . . . .	17
1.5.3	$Z \rightarrow \tau\tau + \text{Jets}$ Background: Embedding Technique . . . . .	19
1.6	Systematic Uncertainties . . . . .	24
1.6.1	Detector-related Systematics Uncertainties . . . . .	24
1.6.2	Theoretical Uncertainties . . . . .	28
1.6.3	$Z/\gamma^* \rightarrow \tau\tau$ Embedding Systematics . . . . .	28
1.6.4	QCD Multi-Jet Systematics . . . . .	30
1.7	Results . . . . .	33
1.7.1	LHC Procedure For Limits Setting . . . . .	33
1.7.2	Exclusion Limits . . . . .	36



# Chapter 1

## Search for neutral MSSM Higgs Bosons in the $A/h/H \rightarrow \tau^+\tau^- \rightarrow e\mu + 4\nu$ decays

Under the light of the recent discovery at LHC of a Higgs boson with mass of 125 GeV [73, 74], remains an open question whether this new particle constitute all the pieces of the Higgs sector or whether it is only one of several bosons predicted in some theories that go beyond the SM. The most recent measurements [75, 76, 77, 78] of its properties shows this new boson to be, within experimental uncertainties, perfectly compatible with the SM Higgs boson, however such a new particle can still be accommodated within several beyond the standard model (BSM) theories, this is particularly true for Super Symmetry.

This chapter presents the search for the neutral MSSM Higgs bosons decaying into pairs of tau leptons in the fully leptonic final state, which is part of the ATLAS publication<sup>1</sup> for the neutral MSSM Higgs boson search []. The search is based on 20.3 fb<sup>-1</sup> of 8 TeV data recorded by the ATLAS experiment during 2012 at the Large Hadron Collider. A brief summary of the MSSM Higgs sector phenomenology is given in section

In section 1.3 an introduction to experimental searches and to the strategy of this particular analysis is given, in section 1.5 the background model estimation is described, while in section 1.6 methods to evaluate systematic uncertainties are discussed, finally in section 1.7 the result of the search are presented.

---

<sup>1</sup>to Sandra: I'll remove this sentence if Conf note won't be ready in time

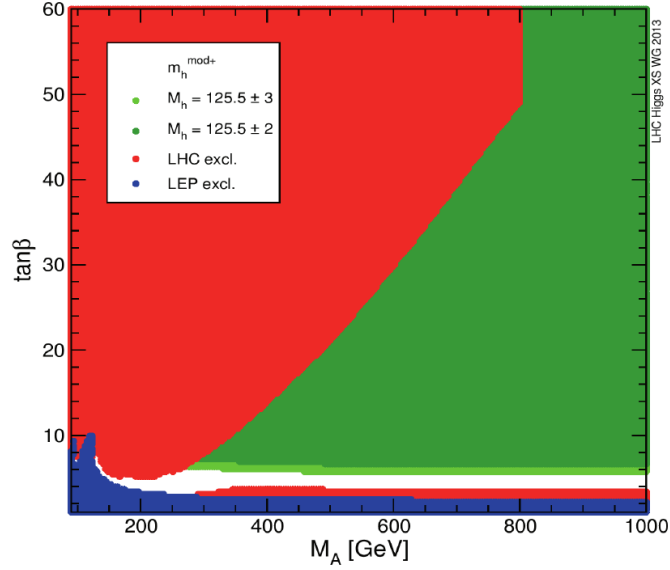


Figure 1.1: Excluded and allowed regions of the  $m_A - \tan\beta$  parameter space for the  $m_h^{mod+}$  benchmark scenario. Excluded regions are determined based on direct Higgs boson searches at LEP (blue) and LHC (red). The two green bands correspond to the parameter regions which are compatible with the assumption that the lightest Higgs boson,  $h$ , has a mass respectively of  $M_h = 125.5 \pm 2$  or  $\pm 3$  GeV. For more detail see [27].

## 1.1 Introduction

In the Minimal Supersymmetric extension of the Standard Model (MSSM) [7, 8] the Higgs sector is composed of two Higgs doublets of opposite hyper-charge, resulting in five observable Higgs bosons: two of these are neutral and  $CP$ -even ( $h, H$ ), one is neutral and  $CP$ -odd ( $A$ ) and two are charged ( $H^\pm$ ). At tree level their properties such as masses, widths and branching ratios can be predicted in terms of only two parameters, often chosen to be the mass of the  $CP$ -odd Higgs boson  $m_A$  and the ratio of the vacuum expectation values of the two Higgs doublets  $\tan\beta$  (for more details see chapter ??). It is impractical for an experimental search to explore the full parameter space of the MSSM, several benchmark scenarios are then introduced by fixing the parameters to typical values for most interesting phenomenology to occur. With the recent Higgs boson discovery, benchmark scenarios of the MSSM have been updated to accommodate for new experimental constraints. As an example, Figure 1.1 shows the currently excluded and allowed regions of the MSSM parameter space for the  $m_h^{mod+}$  updated benchmark scenario. In this scenario a supersymmetric SM-like Higgs boson is assumed with a mass  $m_h = 125$  GeV, large regions of the  $m_A - \tan\beta$  parameter space are compatible with this assumption and remain still unexplored, this is a strong motivation to pursue the search for additional neutral MSSM Higgs bosons.

The MSSM predicts the existence of a Higgs boson with properties that resemble those of a SM Higgs boson in large regions of its parameter space. This is usually the

Figure 1.2: To Sandra: the diagrams are will be updated asap.

case for the lightest Higgs,  $h$ , the other two,  $H$  and  $A$ , tend to be degenerate in mass and decouple from gauge bosons. On the other hand, the couplings of the latter two Higgses with down (up) type fermions are enhanced (suppressed) by  $\tan \beta$ , meaning that for large  $\tan \beta$  bottom-quark and  $\tau$  lepton will play an important role either for production and decay.

The two most relevant production mechanisms for the MSSM Higgs bosons at LHC are gluon-gluon fusion,  $gg \rightarrow A/H/h$  and the production in association with  $b$ -quarks  $pp \rightarrow b(b)A/h/H$ , the latter becoming important for large value of  $\tan \beta$ . Those are the two production mechanism considered in this analysis. The favoured decay mode for the neutral MSSM Higgs bosons is  $b\bar{b}$  (in the assumption that all supersymmetric particle are heavy enough), this is followed, for the CP-odd  $A$  and CP-even  $H$  Higgs bosons, by the decay to  $\tau$  pairs. Given that the former is very difficult to distinguish from the large  $b\bar{b}$  background at the LHC, the decay mode  $A/h/H \rightarrow \tau^+\tau^-$  provides the highest sensitivity for this search.

In the following a search for the neutral MSSM Higgs bosons in the final state  $A/h/H \rightarrow \tau^+\tau^- \rightarrow e\mu + 4\nu$  is presented. This search is complementary to the other  $\tau$  final state searches characterized by the presence of one or two hadronic  $\tau$  decays. Despite the fact that the  $e-\mu$  final state corresponds to a total  $\tau^+\tau^-$  branching ratio of only 6%, this search has a competitive sensitivity with the other  $\tau$  final state, especially for low  $m_A$ . This effect is mainly due to the high transverse momentum requirement at trigger level for hadronic  $\tau$  decay.

## 1.2 Signal and Background Processes

Signal events, in which the neutral MSSM Higgs bosons decays through  $A/h/H \rightarrow \tau^+\tau^- \rightarrow e\mu + 4\nu$ , are characterized by the presence of one electron and one muon of opposite charge, these are isolated and with relatively high transverse momentum, additionally four neutrinos contribute to the missing transverse energy of the event. Figure 1.2 shows leading order Feynman diagram for the two signal production mode considered, gluon-gluon fusion and  $b$ -associated production. The production modes also contributes to the characterization of the signal topology: the presence or the absence of  $b$ -jet in the final state is in fact expected in case of  $b$ -associated or gluon-gluon fusion production mode, respectively.

The signal topology just described is common to several other processes, which unfortunately, have higher cross section than the sought signal. The dominant backgrounds for this search are the production of  $Z/\gamma^* \rightarrow \tau^+\tau^-$  either via Drell-Yan process or in association with jets and the top quark production ( $t\bar{t}$  and single top production is intended). Additional significant backgrounds are diboson production (like  $WW$  or  $ZZ$ ) and events with non-prompt leptons coming solely from hadron decay (QCD multi-jet). Vector bosons production like  $W \rightarrow \ell\nu$  or  $Z \rightarrow \ell\ell$  in association with jets (with  $\ell$  here meaning either  $e$  or  $\mu$ ) are also considered, however these

Figure 1.3: To Sandra: the diagrams are will be updated asap.

Process	Cross-section (pb) [ $\times$ BR]
Signal ( $m_A = 150$ GeV, $\tan \beta = 20$ , $m_h^{max}$ scenario)	
$gg \rightarrow A/h/H \rightarrow \tau\tau \rightarrow e\mu + 4\nu$	0.12/0.09/0.13
$pp \rightarrow b\bar{b}A/h/H \rightarrow \tau\tau \rightarrow e\mu + 4\nu$	0.29/0.03/0.25
Backgrounds	
$W \rightarrow \ell + \text{jets}$	$12.22 \times 10^3$
$Z/\gamma^* \rightarrow \ell\ell + \text{jets}$	$5.5 \times 10^3$
$t\bar{t} \rightarrow \ell\ell + X$	137.3
Single top ( $t$ , $s$ and $Wt$ channels) $\rightarrow \ell + X$	28.4, 1.8, 22.4
Diboson WW, WZ and ZZ $\rightarrow \ell + X$	20.6, 6.8, 1.55

Table 1.1: The cross sections multiplied by the relevant branching ratios (BR) for signal and the considered backgrounds. the symbol  $\ell$  stands for  $\ell = (e, \mu, \tau)$ . Signal cross sections are calculated for the  $m_h^{max}$  scenario shown for  $m_A = 150$  GeV and  $\tan \beta = 20$ , in this case  $m_H = 151$  GeV and  $m_h = 129$  GeV.

processes have a limited impact. Figure 1.3 shows few relevant exaples of leading order Feynman diagrams for the dominant background processes. The production cross sections times the relevant branching fraction for signal and backgrounds are summarised in Table 1.1.

### 1.3 Analysis Strategy

Searches for neutral MSSM Higgs bosons have been performed at LEP [9], the Tevatron [10] and the LHC [11, 12]. In this thesis a search for the MSSM  $A/h/H \rightarrow \tau^+\tau^- \rightarrow e\mu + 4\nu$  is performed. The  $e - \mu$  final state is choosen out of the three possible fully leptonic final state of a  $\tau^+\tau^-$  resonance, since it respresent the 50% of the fully total cases and since for the  $e - e$  and  $\mu - \mu$  case large background contribution are expected not only from  $Z/\gamma^* \rightarrow \tau\tau$  but also from  $Z \rightarrow ee$  and  $Z \rightarrow \mu\mu$ , respectively.

Candidated events are selected based on the topological properties of the Higgs boson production and decay, the events are requires to present one electron and one muon, isolated and of opposite charge. The set of events is divided in two orthogonal category which are optimized separately for the two different production mode considered. In the gluon-gluon fusion category (also called *b-veto* category), the absence of a b-tagged jet is required, the main background in this category is  $Z/\gamma^* \rightarrow \tau\tau$ . In contrast, the presence of a b-tagged jet is required for b-associated production category (also called *b-tag* category), the request of a b-jet suppress the  $Z/\gamma^* \rightarrow \tau\tau$  background,  $t\bar{t}$  and single top production are then the main backgrounds in this category.

The  $A/h/H \rightarrow \tau\tau \rightarrow e\mu + 4\nu$  search is performed in the MSSM  $m_h^{max}$  benchmark

scenario scanning the  $m_A - \tan\beta$  plane in the ranges  $90 \leq m_A \leq 300$  GeV and  $5 < \tan\beta < 60$ , the signal prediction is evaluated by simulation.

The dominant  $Z/\gamma^* \rightarrow \tau\tau$  background is estimated from data via a signal-depleted control sample. QCD multi-jet prediction is also estimated from data since it represents a challenge for MC simulation. The prediction of all the other backgrounds is obtained by means of MC simulation. The background model predictions are validated using different signal-depleted control data samples, good agreement is found.

The systematic uncertainties taken into account for simulated signal and backgrounds arise from uncertainties on cross section calculations and on the modeling of the detector response. For backgrounds that are estimated from data, specific uncertainty are evaluated considering the possible uncertainties of the estimation methods.

The final statistical interpretation of the data is based on the comparison of the observed invariant mass distributions with the expected background and signal+background predictions. Exclusion limits are set by means of a binned likelihood ratio test statistic. The limits are interpreted in the MSSM  $m_h^{\max}$  scenario and evaluated as a function of  $m_A$  and  $\tan\beta$ , furthermore, the limits are interpreted, in a less model depended way, in terms of the cross section for the production of a generic Higgs boson,  $\phi$ , of mass  $m_\phi$ , via the production mode  $pp \rightarrow b\bar{b}\phi$  and  $gg \rightarrow \phi$ .

### 1.3.1 Simulated Event Samples

Signal production via the gluon fusion process,  $gg \rightarrow A/H/h$ , was simulated with POWHEG [23] and the associated  $b\bar{b}A/H/h$  production with SHERPA [24]. The pseudoscalar Higgs boson samples were generated in the mass range from 90 GeV to 300 GeV and at  $\tan\beta = 20$ , the same kinematics are assumed for  $A/h/H$  Higgs bosons decay products and at other  $\tan\beta$  values, appropriate reweighting is applied according to the different cross-sections. The  $m_h^{\max}$  MSSM benchmark scenario [28] is assumed.

The production of  $W$  and  $Z/\gamma^*$  bosons in association with jets was simulated with the ALPGEN [16] generator. The  $t\bar{t}$  process was generated using the POWHEG generator. The single-top (s-channel,  $Wt$ ) processes were generated using MC@NLO [18], while single-top (t-channel) processes were generated with AcerMC [19]. The production of diboson ( $WW$ ,  $WZ$ ,  $ZZ$ ) were generated with HERWIG [20]. For all ALPGEN and MC@NLO samples described above, the parton shower and hadronisation were simulated with HERWIG and the activity of the underlying event with JIMMY [21]. Different parton density functions (PDFs) sets are used depending on the generator - CTEQ6L1 [25] is used by ALPGEN and AcerMC while CT10 [26] is used by SHERPA, POWHEG and MC@NLO.

TAUOLA [30] and PHOTOS [31] are used to model the tau lepton decay and additional photon radiation from charged leptons in the leading-log approximation, respectively, except for SHERPA samples.

All MC event samples were passed through the full simulation of the ATLAS detector using GEANT4 [32, 33] The effects of the simultaneous recording of several events from the same or neighbouring bunch crossings (pile-up) are considered in

Channel	Selection
Preselection	Trigger At least one reconstructed vertex Event cleaning Tau Veto Exactly one tight isolated electron with $P_T > 15$ or 25 GeV (trigger dependent) Exactly one Combined isolated muon with $P_T > 10$ GeV Opposite charge between the leptons
b-Tag	Exactly one b-tagged taggable jet $\Delta\phi(e - \mu) > 2$ $\sum \cos \Delta\phi > -0.2$ $\sum H_T < 100$ GeV $\sum L_T + E_T^{miss} < 100$ GeV Good MMC solution
b-Veto	Exactly zero b-tagged taggable jets $\Delta\phi(e - \mu) > 1.6$ $\sum \cos \Delta\phi > -0.4$ Good MMC solution

Table 1.2: Summary of the preselection and the full selections used for the b-tag and b-veto channels.

the simulation.

## 1.4 Event Selections and Categorization

Data quality requirement according to [61] recommend to not use event with jet activity in

According to the signal events characteristics, each event either data and MC should satisfy the following selection criteria, these selections are shared by both analysis category and therefore referred in the following as “common selections”:

- (i) Trigger requiring the presence of an electron with  $P_T > 24$  GeV, or alternatively, an electron with  $P_T > 12$  GeV together with a muon with  $P_T > 8$  GeV.  
*Note to Sandra: should I mention that the trigger is a selection during data taking? Or is the trigger is supposed common knowledge?*
- (ii) Exactly one reconstructed electron and one muon of opposite charge should be present in the event. The muon is required to have  $P_T > 10$  GeV, while the electron should have  $P_T > 15$  or 25 GeV depending on the trigger that selected the event. For definition of reconstructed electron and muon object see chapter ??.
- (iii) The two leptons should be isolated, meaning that in a cone around the lepton there should be little energy deposit (should not be surrounded by other particle, common of non-prompt leptons coming from jets). For more detail about isolation properties see section 1.5.



- (iv) The events is rejected if at least one jet from hadronic  $\tau$  decay is found with  $P_T > 15$  GeV.
- (v) The invariant mass of the sum of the electron and muon 4-vectors should be greather than 30 GeV.

This set of selection all togheter are referred in the following as *preselection*. More detail on preselections are reported in table 1.2, for details on object reconstruction and quality requirements see chapter ???. The two analysis category, *b-tag* and *b-veto*, are defined adding on top of the preselections the request of "exactly one b-tagged jet" or "no b-tagged jet" in the event respectively, to be *taggable* a jet should have  $P_T > 20$  GeV and  $|\eta| < 2.5$ .

### Event Category

The final state of Higgs decaying into tau pair coincide with the one from  $Z/\gamma^* \rightarrow \tau\tau$  process, this is then an irreducible background. Exploiting the different kinematics of the Higgs decay with respect to other backgrounds it possible to disentangle between the two. In the Higgs decaying into  $\tau^+\tau^- \rightarrow e\mu + 4\nu$  the taus are highly boosted and this feature is transferred to the final state leptons, their kinematics then result to be significantly different with respect to process like diboson or  $t\bar{t}$ . A first difference is that  $e$  and  $\mu$  from the Higgs decay will be more likely "back-to-back", as it is shown in Figure 1.4(a) where the angle between the leptons in the transverse plane  $\Delta\phi = |\phi_e - \phi_\mu|$  is reported. Furthermore the neutrinos will be more likely collinear with the charged leptons: this feature can be matematically seen as the sum of scalar product between missing energy and the leptons four-vectors in the transverse plane, if the vectors are normalised to unit versors then what remains is a relation only between angles:

$$\hat{E}_T^{miss} \cdot (\hat{P}_T^\mu + \hat{P}_T^e) = \cos(\Delta\phi_{E_T,\mu}) + \cos(\Delta\phi_{E_T,e}) = \sum_{\ell} \cos(\Delta\phi_{E_T,\ell})$$

collinearity implies this sum to be equal to zero as it is shown in Figure 1.4(b). These two feature can be used to distinguish between mu-e coming from decay from highly boosted object and the one coming from W decays in top or in dibosons backgrounds which will have a more spread distribution. In b-veto category these two variables are sufficient to suppress contribution from dibosons, no other selection is applied in this category because it has been shown to not bring significant improvement.

In the b-tag category the situation is different, the request of b-jet enhance backgrounds with high jet activity as top production, given the relatively low jet activity of Higgs events (also in the case of b-associated production) it is possible to separate them from top production which instead is very likely to have two or more highly enegetic jets in the event. Little jet activity is achieved by requesting the sum of the jets  $P_T$  in the event to be small, this variable is called  $H_T$  and is shown in Figure 1.4(c). Another feature that distinguish top pair production from Higgs is the much higher invariant mass of the former final state, in the transverse plane all the leptons will tend to have a higher momentum, the sum of

lepton  $P_T$  and  $E_T^{miss}$  is then used as a discriminating variable. Figure 1.4(d) shows the distribution of this last analysis variable.

The above described variables defines the signal region in the b-tag and b-veto category, in table 1.2 a summary of the preselection and all the selection variable used with their optimized cut values is reported. Figure 1.5 shows the final state invariant mass distribution (here the  $MMC_{mass}$  discriminating variable is used see section 1.4.1) as a function of the selection stage, while in tables 1.4-1.3 the number of events that survives at each cut stage for different background is reported.

### 1.4.1 Mass Reconstruction with MMC Technique

Accurate invariant mass reconstruction of a di- $\tau$  resonance is a challenging task due to the presence of neutrinos from the  $\tau$  leptons decay. In case of leptonic decay of both  $\tau$  leptons a pair of neutrinos for each of them are involved in the final state, the system presents then eight unknowns, which corresponds to the four-momentum of the neutrinos pairs. Four additional kinematic constraints are set by the following equations:

$$\begin{aligned} \vec{E}_T^{miss} &= \vec{P}_T^{mis_1} + \vec{P}_T^{mis_2} \\ M_{\tau_i}^2 &= m_{mis_i}^2 + m_{vis_i}^2 + 2\mathbf{P}_{vis_i} \cdot \mathbf{P}_{mis_i} \end{aligned} \quad (1.1)$$

where the index  $i$  runs over the two  $\tau$  leptons of the event and assumes the values of 1 or 2,  $\vec{P}_T^{mis_i}$ ,  $m_{mis_i}$  and  $\mathbf{P}_{mis_i}$  are respectively the transverse momentum, the invariant mass and the four momentum of the pair of neutrinos related to the  $\tau$  lepton decay  $i$  with mass  $M_\tau$ , the subscript  $vis$  indicates invariant quantities related to the charged lepton from  $\tau$  lepton decay. The system has still four degrees of freedom, several approximations are possible to further constrain the momentum carried by neutrinos, for example assuming them collinear to the electron or muon from  $\tau$  lepton decay, however those approximations suffer from mass resolution limitations.

In this analysis, the so-called "Missing Mass Calculator" (MMC) algorithm is used to calculate the most likely di- $\tau$  system invariant mass given the event topology, the implementation of the method in this search is based on [79]. The concept of the MMC is to solve equation 1.1 assigning values to the yet undetermined variables, performing a "scan" over a four dimensional parameter space. The four independent variables are chosen to be  $m_{mis_i}^2$  and  $\cos\theta_i^*$ , the latter defined as the angle between the charged lepton from the  $\tau$  lepton decay and the boost direction of the  $\tau$  lepton. The di- $\tau$  invariant mass of the event can be calculated for each given point of the parameter space that solves equations 1.1, however, the solutions are not all equally likely and the probability of a given  $\tau$  decay configuration can be predicted by means of simulation (PYTHIA supplemented with TAUOLA package is used). Each point in the parameter space, corresponding to a particular di- $\tau$  invariant mass, is then weighted by its probability to occur. The estimator for the final discriminant, the mass of the di-tau system  $MMC_{mass}$ , is the maximum of the weighted invariant mass distribution calculated for the scanned points.

The missing energy plays an important role in the MMC method and its resolution has an impact on the calculation of the invariant mass. To improve  $E_T^{miss}$  resolution, a scan over a six dimensional parameter space is performed in a similar

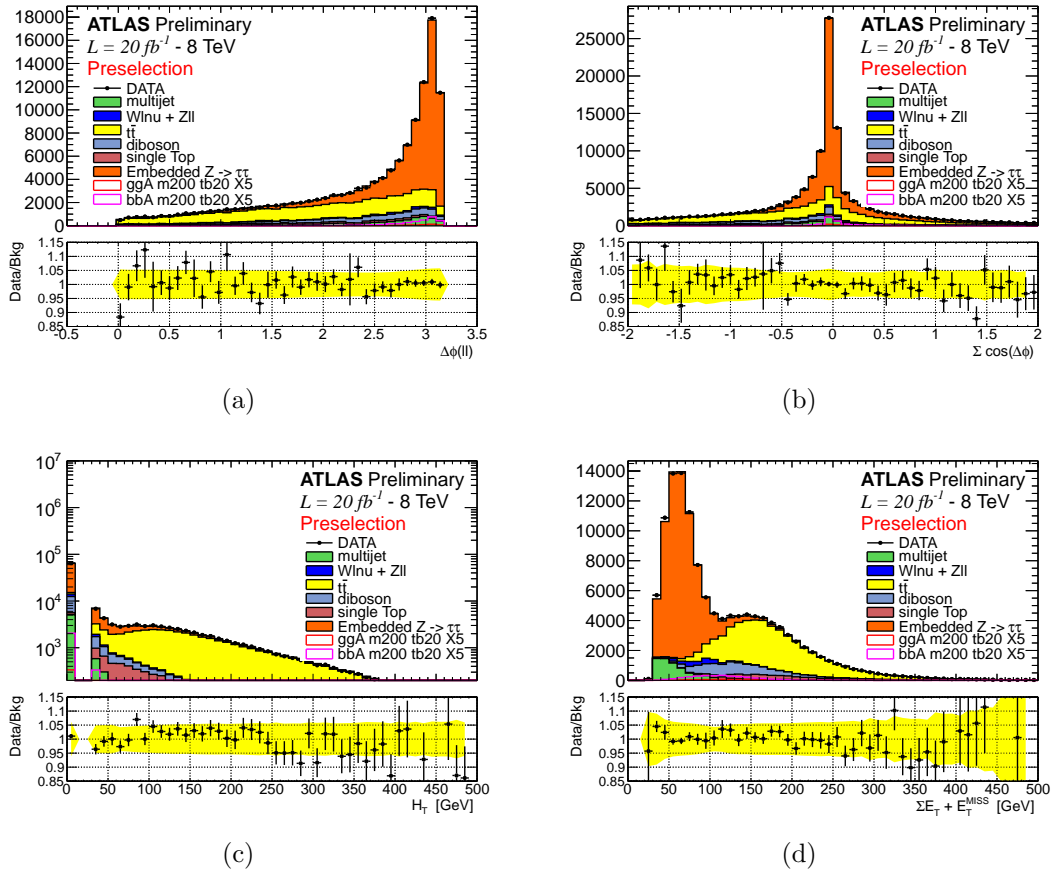


Figure 1.4: Distribution of analysis variable after preselection.

way as described above, in this case however,  $\vec{E}_T^{miss}$  is also considered unknown and value are assigned to it according to its uncertainty. The probability of each solution is calculated and the final missing transverse energy is given by the weighted mean of the scanned points.

The final procedure consist in obtaining first an estimated for  $E_T^{miss}$  by means of a six dimensional scan over the solution of equations 1.1, successively a four dimensional scan is performed fixing  $E_T^{miss}$  to the updated value and calculating the most likely invariant mass of the di- $\tau$  system. Figure.....

## 1.5 Background Modeling and Validation

This section describes the strategies for background modeling and validation. Monte Carlo (MC) simulation is extensively used for model either background and signal, in section ?? a brief description of the simulated sample used is given.

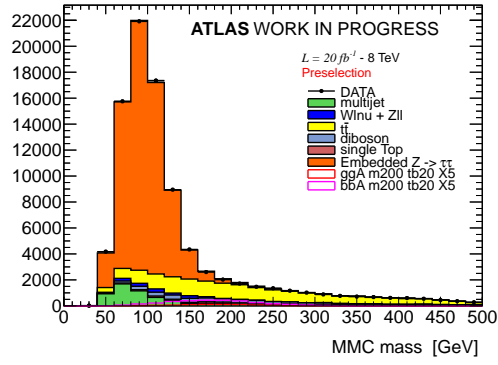
Monte Carlo simulations of any process are usually prone to systematics uncertainties due to non-perfect descriptions of pileup effects, underlying event and detector performance, therefore, data-driven background estimation method are employed for the estimate of  $Z/\gamma^* \rightarrow \tau\tau$  and QCD multijet backgrounds, described respectively in section 1.5.3 and 1.5.2. Other background processes, such as  $t\bar{t}$ , single top, dibosons,  $Z \rightarrow ll + \text{jets}$  (where  $l = e, \mu$ ) and  $W + \text{jets}$ , are estimated using MC predictions. Given the particular importance of  $t\bar{t}$  a dedicated study to validate this background has been made and described in section 1.5.1.

In this section we make use of analysis tools, quality requirements and object definition (like electrons, jet and muon) described in chapter ?. Furthermore a set corrections is applied to simulated events to take into the non perfect description of detector performance and response, full detail on those corrections is reported in appendix ?. Systematic uncertainties on the background model predictions are detailed in Section 1.6.

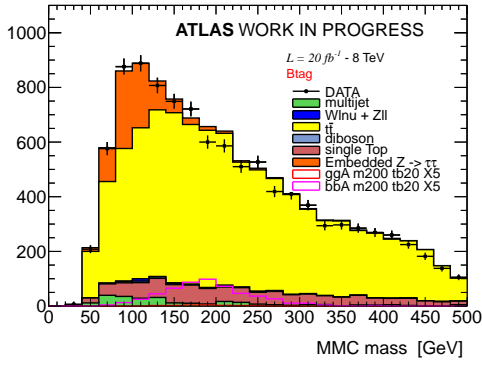
A good agreement between data and background model is found after preselections, this is supported by figure 1.6 which shows few kinematic variables and figure 1.4 which shows analysis selection variables after preselection.

### 1.5.1 Top Quark Pair Production Validation

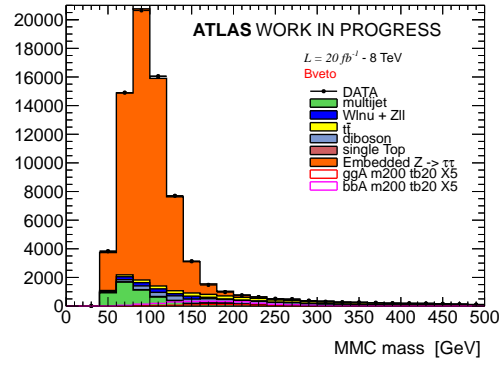
The background from top quark pair production is estimated using a sample of events from the POWHEG-PYTHIA MC generator. Since this is one of the major backgrounds for this analysis a careful validation is needed, for this purpose a  $t\bar{t}$  rich control region is defined using events passing the preselection with the additional requirement of two b-tagged jets. Figures 1.7 and 1.8 show a set of kinematic and analysis selection variables in this CR, for both data and the MC prediction, good agreement between data and the background model is found: an overall data to background ratio of  $0.998 \pm 0.011(\text{stat.}) \pm 0.110(\text{sys.})$  is observed. The total systematic uncertainty on the ratio is dominated by the uncertainty on the b-tagging efficiency.



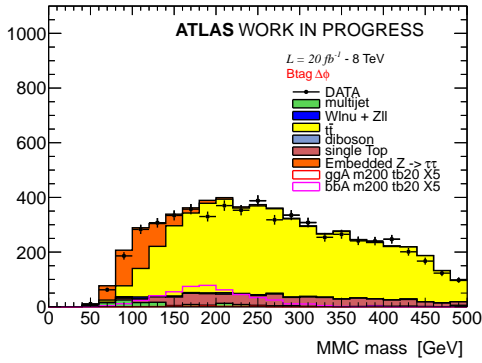
(a)



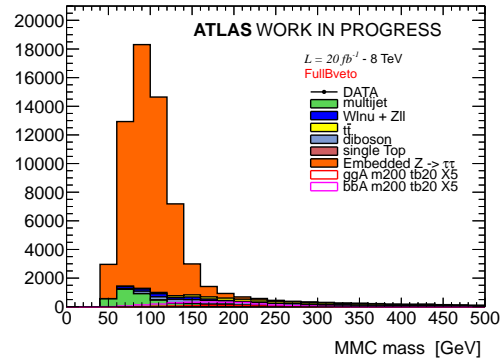
(b)



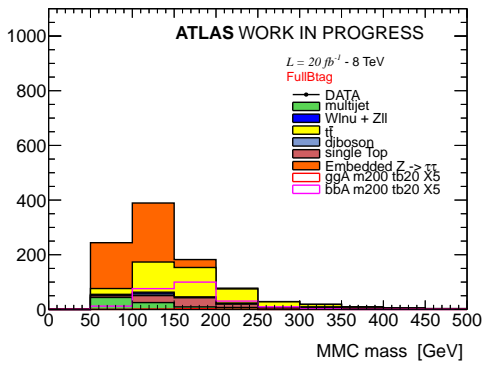
(c)



(d)



(e)



(f)

Figure 1.5: Distribution of the  $MMC_{mass}$  for different cuts stage, see text. Left column corresponds to b-tag category, right column to b-veto.

	Preselection	n(b-jet)=1	$\Delta\phi(e-\mu) > 2$	$\sum \cos \Delta\phi > -0.2$	$\sum L_T + E_T^{miss} < 100 \text{ GeV}$	$\sum H_T < 100 \text{ GeV}$	mmc
Data	125886	23352	-	-	-	-	-
Multijet	6700 $\pm$ 500	330 $\pm$ 40	208 $\pm$ 27	135 $\pm$ 22	114 $\pm$ 17	100 $\pm$ 15	100 $\pm$ 15
$Z \rightarrow \ell\ell$	570 $\pm$ 50	5.2 $\pm$ 1.8	2.3 $\pm$ 1.1	2.3 $\pm$ 1.1	1.7 $\pm$ 1.0	0.9 $\pm$ 0.8	0.9 $\pm$ 0.8
$W \rightarrow \ell\nu$	1630 $\pm$ 150	20 $\pm$ 6	15 $\pm$ 6	13 $\pm$ 6	10 $\pm$ 6	10 $\pm$ 6	10 $\pm$ 6
Diboson	9340 $\pm$ 50	99 $\pm$ 5	63 $\pm$ 4	36.4 $\pm$ 3.0	14.8 $\pm$ 1.8	13.3 $\pm$ 1.8	13.1 $\pm$ 1.8
$t\bar{t}$	40630 $\pm$ 110	19810 $\pm$ 70	9680 $\pm$ 50	6450 $\pm$ 50	808 $\pm$ 15	350 $\pm$ 10	330 $\pm$ 10
Single Top	4450 $\pm$ 40	2456 $\pm$ 33	1223 $\pm$ 23	784 $\pm$ 18	122 $\pm$ 7	99 $\pm$ 7	90 $\pm$ 6
$Z/\gamma^* \rightarrow \tau\tau$	61500 $\pm$ 70	952 $\pm$ 9	625 $\pm$ 7	540 $\pm$ 7	482 $\pm$ 6	421 $\pm$ 6	418 $\pm$ 6
Signal			-	-	-	-	-

Table 1.3: Number of data and background events in the b-tag channel.

	Preselection	n(b-jet)=0	$\Delta\phi(e - \mu) > 1.6$	$\sum \cos \Delta\phi > -0.4$	mmc
Data	125886	89155	-	-	-
Multijet	6693 $\pm$ 456	6357 $\pm$ 461	5322 $\pm$ 438	4137 $\pm$ 339	3934 $\pm$ 335
$Z \rightarrow \ell\ell$	569 $\pm$ 48	564 $\pm$ 48	516 $\pm$ 47	434 $\pm$ 44	432 $\pm$ 44
$W \rightarrow \ell\nu$	1625 $\pm$ 155	1604 $\pm$ 155	1145 $\pm$ 125	714 $\pm$ 101	656 $\pm$ 100
Diboson	9338 $\pm$ 48	9235 $\pm$ 48	7358 $\pm$ 43	4002 $\pm$ 31	2925 $\pm$ 27
$t\bar{t}$	40632 $\pm$ 106	7707 $\pm$ 46	5044 $\pm$ 37	3416 $\pm$ 31	2159 $\pm$ 24
Single Top	4449 $\pm$ 44	1664 $\pm$ 27	1124 $\pm$ 22	682 $\pm$ 18	435 $\pm$ 14
$Z/\gamma^* \rightarrow \tau\tau$	61503 $\pm$ 68	60440 $\pm$ 67	58078 $\pm$ 65	55303 $\pm$ 64	54683 $\pm$ 63
Signal			-	-	-

Table 1.4: Number of data and background events in the b-veto channel.

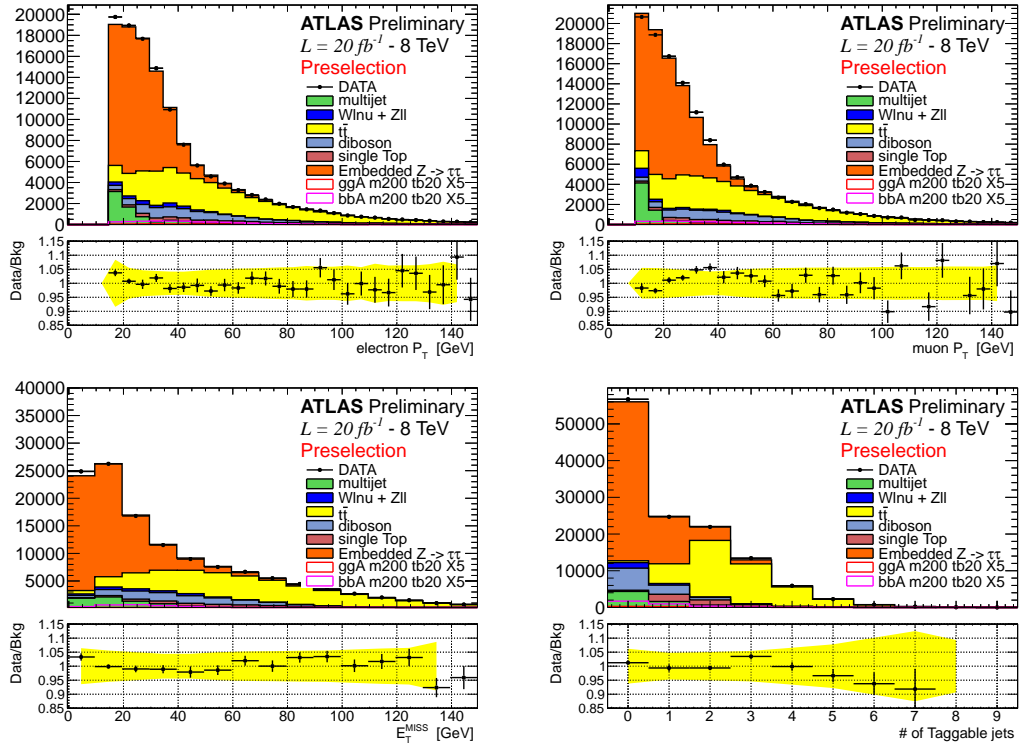


Figure 1.6: Distribution of some kinematic variables after preselection.

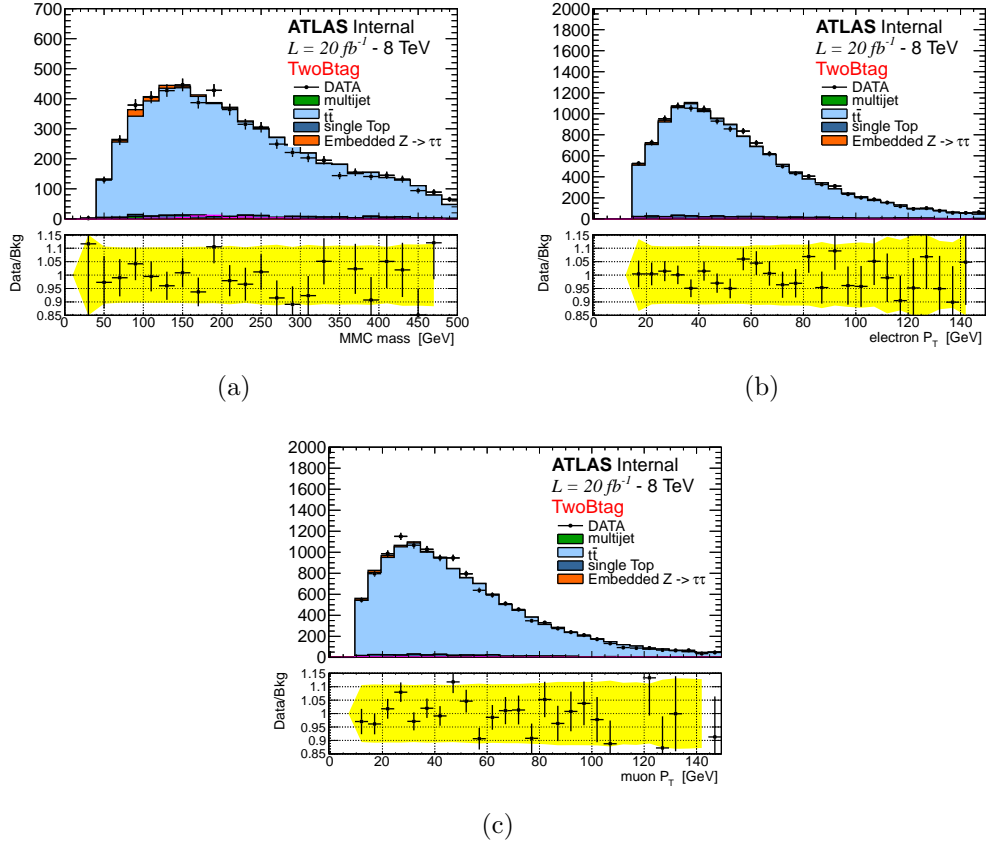


Figure 1.7: Distributions of a) the MMC mass, b) the transverse momentum of the electron  $P_T(e)$  and c) the transverse momentum of the muon  $P_T(\mu)$ , for both data and MC in the  $t\bar{t}$  control region. The uncertainties on the points for the ratio plot show the statistical uncertainty on the data to background ratio, whereas the yellow band show the total systematic uncertainty on this ratio.



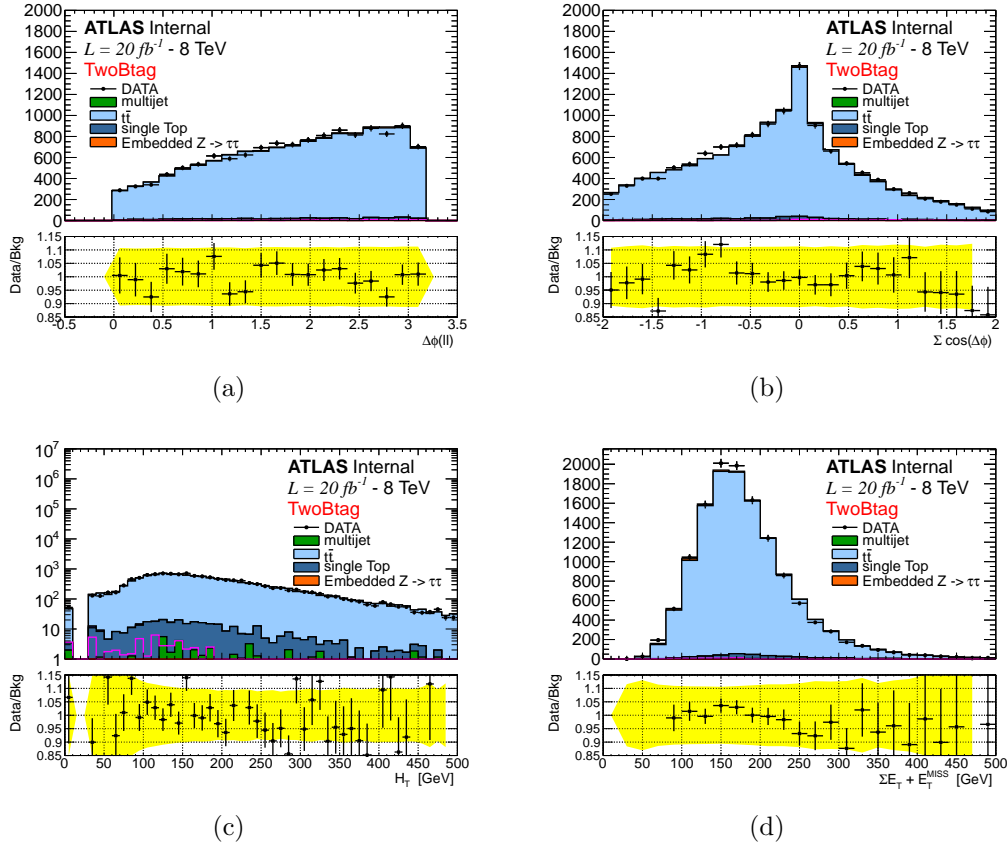


Figure 1.8: Distributions of a)  $\Delta\phi(e - \mu)$ , b)  $\Sigma \cos \Delta\phi$ , c)  $\Sigma L_T + E_T^{\text{miss}}$  and d)  $H_T$ , for both data and MC in the  $t\bar{t}$  control region. The uncertainty on the points for the ratio plot show the statistical uncertainty on the data to background ratio, whereas the yellow band show the total systematic uncertainty on this ratio.

### 1.5.2 Multi-jet Background

The QCD multi-jet background represents an important background, especially in the b-veto category, due to its high cross-section and the relatively low cut on lepton  $P_T$  used in this analysis. This background is evaluated by a data-driven technique, the so-called ABCD method. The ABCD method consists of splitting the data sample in four regions: the signal region (SR) and three control regions (CR), where the control regions are mutually orthogonal and designed to be enriched in multi-jets events. The four regions are defined by using the charge correlation between the leptons and isolation selections. With isolation is intended the sum of the energy deposit in a cone of fixed size around the lepton, this variable can be defined using calorimetric energy deposition or track momentum measurement done by the inner detector. To obtain regions rich in multi-jet background, the selections on both the calorimetric and tracking isolation are inverted with respect to the nominal ones defining anti-isolated leptons, is then possible to define four regions: opposite sign (OS) or same sign (SS) with respectively isolated or anti-isolated leptons. Historically the letters A-D are assigned to this regions for a

Region	Lepton Charge	Lepton Isolation
A (signal region)	OS	isolated
B	SS	isolated
C	OS	anti-isolated
D	SS	anti-isolated

Table 1.5: QCD background estimation control regions, defined by having leptons with opposite signs (OS) or same signs (SS) and by having the leptons either isolated or anti-isolated.

quicker reference as defined in Table 1.5.

An assumption of the ABCD method is that multi-jet backgrounds populate the OS and SS events independently of lepton isolation criteria, or in other words that the ratio of OS/SS events is uncorrelated with the lepton isolation selections. In this case, the number of QCD events in the signal region  $A$  can be estimated from the yield of multijet events in the control regions  $B$ ,  $C$  and  $D$ , using the equation

$$N_A = N_B \times \frac{N_C}{N_D} = N_B \times R_{QCD} \quad (1.2)$$

To obtain the multijet yields in the data CRs, the contamination from electroweak (W+jets, Z+jets and dibosons) and top processes ( $t\bar{t}$  and single top production) are subtracted in each control region using the MC prediction for their event yield. Tables 1.6 and 1.7 show the event yield for each CR throughout the full cut-flows along with the predictions of non-QCD multi-jets events which are subtracted. Signal contamination has been checked in all the three control regions for different mass points. For the range of  $m_A$  and  $\tan\beta$  considered in this analysis, the highest signal contamination is seen in region B for the mass point  $m_A = 300$  GeV and  $\tan\beta = 50$ , where a contamination of 0.2% is observed<sup>2</sup>.

Shapes of kinematic distributions for QCD events are taken from region B, this region is expected to have similar kinematic property to the SR, however, suffers of either lower statistics and higher contamination with respect to region C or D. This choice is made to avoid a shape bias due to isolation requirements at trigger level (only the single-electron trigger ask for isolation), figure 1.9 shows the comparison between the electron  $P_T$  distributions in region B and D, in the latter high  $P_T$  electrons are suppressed, they do not pass trigger selections. Eventually the trigger isolation requirement could bias also the ratio OS/SS, this possibility has been checked carefully in a dedicated study and reported in Appendix ?? : to a good approximation, such trigger effects cancel out in the ratio OS/SS and no additional systematic is needed.

To test the ABCD method predictions an additional control region has been defined with the following selections:

- $E_T^{miss} < 20$  GeV
- $H_T < 70$  GeV and  $\sum L_T + E_T^{miss} < 50$  GeV

<sup>2</sup> This value is mainly due to b-associated production and, as it scales with the cross section, for  $\tan\beta = 20$  would be an order of magnitude smaller.

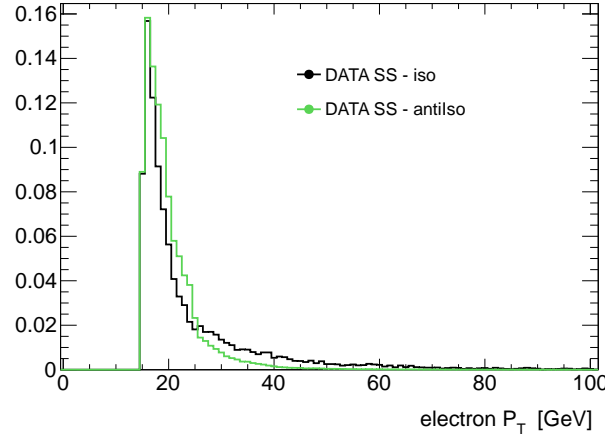


Figure 1.9: Comparison of the electron  $P_T$  distribution in region B and region D, showing the bias due to the trigger. The histograms are normalised to the same area.

- $0 < MMC_{mass} < 80$  GeV

This control region is designed to enhance multi-jet background with respect to  $Z/\gamma^* \rightarrow \tau\tau$  keeping the final state kinematics as similar as possible to the SR. Figure 1.10 shows the  $MMC_{mass}$  distribution for this CR with and without b-tagging requirements, agreement between data and the background model is found within statistical and detector related systematics uncertainty.

Systematic uncertainties are assigned on the scaling factor  $R_{QCD}$  and on the shape of the discriminating variable  $MMC_{mass}$  to take into account any correlation between isolation and charge of the leptons, details on the systematic uncertainty evaluation are addressed in Section 1.6.

### 1.5.3 $Z \rightarrow \tau\tau + \text{Jets}$ Background: Embedding Technique

The background from  $Z/\gamma^* \rightarrow \tau\tau$  decays is the major background to this analysis, a good understanding of it is then crucial. Unfortunately, for a light Higgs boson, it is impossible to completely separate  $Z/\gamma^* \rightarrow \tau\tau$  decays from the signal and a signal free data control region cannot be defined. However, thanks to the small Higgs coupling to muons,  $Z \rightarrow \mu\mu$  decays provide a good starting point to model  $Z/\gamma^* \rightarrow \tau\tau$  events in a data-driven way. An hybrid Data-MC sample, known as "Embedding" is used to model the  $Z/\gamma^* \rightarrow \tau\tau$  background:  $Z \rightarrow \mu\mu$  candidates are selected in data, then, the two muons from the  $Z$  decay are substituted with the decay products from simulated taus, this means that the energy deposit and tracks in a cone around the muon are subtracted and substituted with the one from  $\tau$  decay, those taus have the same kinematics as the original muons. Further details on this technique may be found in [34, 35].

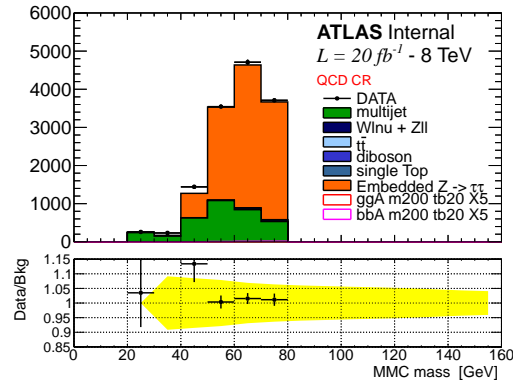
Trigger is not simulated in the embedding samples, the event yield is normalised to ALPGEN  $Z/\gamma^* \rightarrow \tau\tau$  at preselection stage. Furthermore a set of corrections, as described in [36], are applied to unfold from the original  $Z \rightarrow \mu\mu$  trigger and

Selection		B	C	D	$R_{QCD}$
Preselection	Data	6189	604628	312901	$1.929 \pm 0.004$
	non-QCD	$2510 \pm 180$	$1090 \pm 30$	$730 \pm 35$	
B-tag	Data	419	44619	27257	$1.64 \pm 0.01$
	non-QCD	$215 \pm 10$	$310 \pm 12$	$277 \pm 13$	
$\Delta\phi(e - \mu)$	Data	230	38810	23316	$1.67 \pm 0.01$
	non-QCD	$104 \pm 6$	$200 \pm 10$	$175 \pm 7$	
$\sum \cos \Delta\phi$	Data	149	31379	18779	$1.67 \pm 0.02$
	non-QCD	$67 \pm 5$	$127 \pm 8$	$114 \pm 6$	
$\sum H_T$	Data	83	27781	15626	$1.78 \pm 0.02$
	non-QCD	$23 \pm 4$	$25 \pm 3$	$22 \pm 3$	
$\sum L_T + E_T^{miss}$	Data	71	27735	15590	$1.78 \pm 0.02$
	non-QCD	$10 \pm 3$	$22 \pm 3$	$18 \pm 2$	
$MMC_{mass} > 0.$	Data	70	27634	15522	$1.78 \pm 0.02$
	non-QCD	$9 \pm 3$	$20 \pm 3$	$17 \pm 2$	

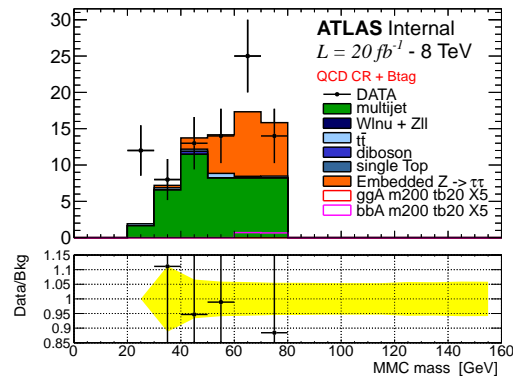
Table 1.6: QCD background estimation as a function of the analysis selections for the b-tagged category. The yields for the different control regions, as well as the scaling factor  $R_{QCD}$ , are reported. The error on the  $R_{QCD}$  is statistical only.

Selection		B	C	D	$R_{QCD}$
Preselection	Data	6189	604628	312901	$1.929 \pm 0.004$
	non-QCD	$2510 \pm 180$	$1090 \pm 30$	$730 \pm 35$	
B-veto	Data	5673	558217	284847	$1.960 \pm 0.004$
	non-QCD	$2220 \pm 180$	$710 \pm 30$	$415 \pm 30$	
$\Delta\phi(e - \mu)i$	Data	4610	532583	271404	$1.962 \pm 0.005$
	non-QCD	$1700 \pm 170$	$580 \pm 30$	$345 \pm 30$	
$\sum \cos \Delta\phi$	Data	3417	486747	247712	$1.965 \pm 0.005$
	non-QCD	$1120 \pm 100$	$370 \pm 20$	$230 \pm 20$	
$MMC_{mass} > 0.$	Data	3177	479967	244276	$1.965 \pm 0.005$
	non-QCD	$1000 \pm 100$	$300 \pm 17$	$190 \pm 20$	

Table 1.7: QCD background estimation as a function of the analysis selections for b-veto category. The yields for the different control regions, as well as the scaling factor  $R_{QCD}$ , are reported. The error on the  $R_{QCD}$  is statistical only.



(a)



(b)

Figure 1.10:  $MMC_{mass}$  distribution for QCD cross check regions defined in section 1.5.2 (a) and for the same CR when in addition one b-tagged jet is required (b).

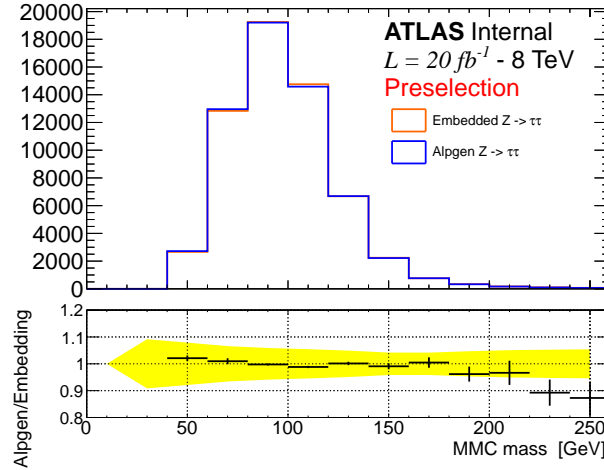


Figure 1.11: Comparison between the embedded  $Z/\gamma^* \rightarrow \tau\tau$  and ALPGEN for  $MMC_{mass}$  distributions.

reconstruction efficiency, then trigger and reconstruction efficiency for a  $e - \mu$  final state are emulated by means of event weight.

The Embedding technique has been validated in several studies, detailed in [34, 36], which show a good description of data and  $Z/\gamma^* \rightarrow \tau\tau$  MC by Embedding. In the context of this analysis, figures 1.11 and 1.12 show comparisons of various kinematic variables between data, embedding and ALPGEN  $Z/\gamma^* \rightarrow \tau\tau$  events at preselection. No significant deviation is seen between the  $MMC_{mass}$  distribution of the embedding and ALPGEN samples, however other relevant variables for this analysis, such as the  $E_T^{miss}$  and the number of b-jets, are slightly better described by embedding.

The Embedding sample is based on selecting  $Z \rightarrow \mu\mu$  candidates in data, the selections assure a rather pure  $Z \rightarrow \mu\mu$  sample, however further selections used in this analysis, for example the b-tagging requirements, could enhance the contamination fraction from other processes. Dedicated studies have been made to estimate the  $t\bar{t}$  and QCD multi-jet contamination in the embedding sample. The  $t\bar{t}$  contamination is estimated by evaluating the embedding yield in a two b-tag control region (as described in Section 1.5.1), these events are assumed to be solely from  $t\bar{t}$  and their yield in the signal region is extrapolated using MC simulation. Table 1.8 shows a summary for the top contamination in embedding. The multi-jet contamination can be estimated starting from the embedding yield in (ABCD) region C, assuming all events in this CR as QCD multi-jet events, the contamination in the SR can be estimated by means of the ABCD method (see Section 1.5.2). The  $R_{QCD}$  factor, in this case, is evaluated using a  $\mu - \mu$  final state with same kinematic selections as for embedding  $Z \rightarrow \mu\mu$  candidate. Table 1.9 shows the estimated contamination of QCD multi-jet in embedding. We consider contamination effects negligible.

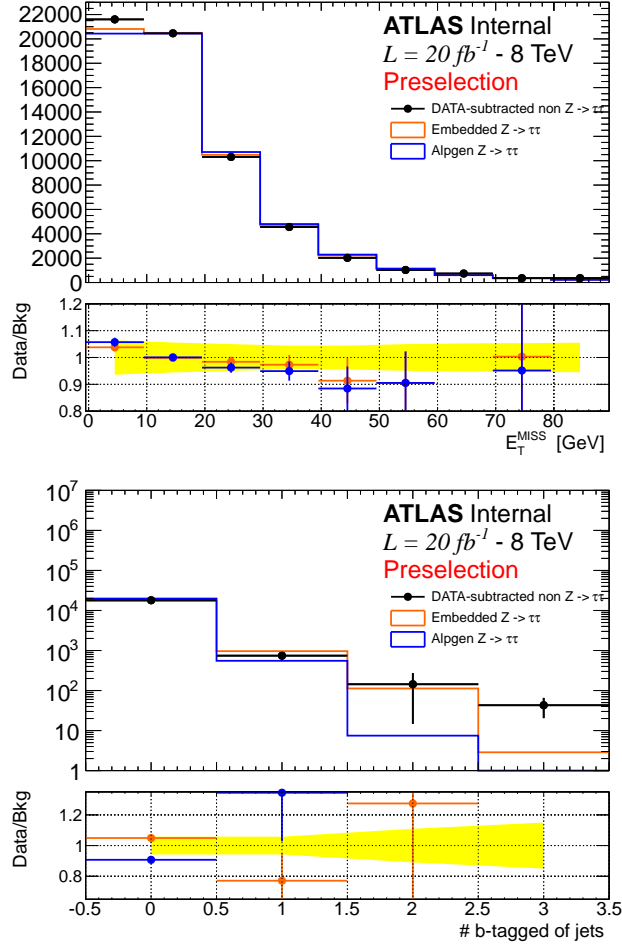


Figure 1.12: Comparison between embedded  $Z/\gamma^* \rightarrow \tau\tau$  and ALPGEN for  $E_T^{\text{miss}}$  and the number of b-tagged jets distributions. Data are superimposed, with the contribution of non- $Z/\gamma^* \rightarrow \tau\tau$  are subtracted.

	Embedding yield in CR	Transfer factor	Estimated events in SR	Contamination
b-tag	$84 \pm 9$	$(2.6 \pm 0.1) \times 10^{-2}$	$2.2 \pm 0.2$	0.5 %
b-veto	$84 \pm 9$	$(1.74 \pm 0.02) \times 10^{-1}$	$15 \pm 2$	0.03 %

Table 1.8: Evaluating embedding  $t\bar{t}$  contamination using a two b-tag CR. The transfer factor is the multiplicative factor that allows to estimate events in SR from the CR.

	Embedding yield in CR	Transfer factor	Estimated events in SR	Contamination
B-tag	$12 \pm 3$	$(7 \pm 1) \times 10^{-3}$	$(8.4 \pm 0.3) \times 10^{-2}$	0.03 %
B-veto	$390 \pm 20$	$(2.5 \pm 0.1) \times 10^{-2}$	$10.0 \pm 0.5$	0.02 %

Table 1.9: Evaluating embedding contamination due to QCD multi-jet using ABCD method, the CR here is with OS anti-isolated events (region C). The transfer factor is the multiplicative factor that allows to estimate events in SR from the CR, in this case is  $N_B/N_D$  and is evaluated using mu-mu final state with the same kinematic selection used in the definition of the embedding sample.

## 1.6 Systematic Uncertainties

This section describes the range of systematic uncertainties that are relevant for this analysis. To account for differences in the detector responses between simulation and data a set of corrections are applied either at object reconstruction level and at event level, the uncertainties on such corrections are considered as detector-related systematic uncertainties and are detailed in section 1.6.1. For samples which rely on MC simulation, theory-related systematics, which include uncertainties on the cross-section and uncertainties on the acceptance of analysis selections, are described in section 1.6.2. Further systematic uncertainties related to data-driven methods for backgrounds estimation are described in section 1.6.3 and 1.6.4.

Each single systematic can contribute separately to the uncertainty on the final event yield and on the shape of the  $MMC_{mass}$  distribution which is used as discriminating variable in limit derivation. Shape systematics are documented in appendix ??, they are found to be negligible for all the samples except Embedding, for which significant deviation are found only in the b-veto category. Systematic uncertainties that do not effect the mass shape distribution and have an impact on the event yield of less than 0.5% (per sample) are neglected in the final limit calculations.

### 1.6.1 Detector-related Systematics Uncertainties

Here systematic uncertainty related to object reconstruction and event corrections are addressed, those corrections are based on the measure of some relevant parameter, each of those parameters correspond to a "nuisance parameter" in our probability model as described in Section ?. Each parameter is varied independently (one sigma up or down) according with its uncertainty and the impact on the analysis yield for each sample is evaluated. In the following, detector related uncertainty are described with some more details, table 1.10 and 1.11 briefly summarize the impact on the samples yield for the most significant systematic uncertainty considered.

**Luminosity** The integrated luminosity of the 8 TeV data recorded at ATLAS during 2012 is measured to be  $20.3 \text{ fb}^{-1}$  [87], its uncertainty is 2.8%.



**Pileup** Simulated events are re-weighted to reproduce the average interactions per bunch crossing,  $\langle \mu \rangle$ , seen in data. Those event weights has an uncertainty wich is propagated to each simulated sample.

**Trigger Efficiency** is corrected in simulation to match (as a mean value) the one in data, those correction weights are evaluated as a function of  $P_T$  and  $\eta$  of the leptons and have assciated uncertainties. Systematic uncertainties on both the single electron and electron-muon trigger efficiency are considered independently, those uncertainty range aproximately 1-2%.

In the embedding sample, the trigger is emulated by applying weights to the event topology in order to recover the right trigger efficiency, those weights are related to the one just described above and have similar uncertainty. Trigger efficiency uncertainty for Embedding are considered uncorrelated with the one of other samples.

**Electrons** Two types of uncertainty on reconstructed electron objects are considered: the first are related to electron identification and reconstruction efficiencies ("Electron ID"), the second type are related to electron energy scale and resolution corrections. The energy scale uncertainties are split into a set of six different nuisance parameters, however, only few of them give a non negligible contribution. Two of them are found to effect the shape of the  $MMC_{mass}$  distribution and are considered independently, those are the uncertainty that arise from the  $Z \rightarrow ee$  momentum measurement ("Electron Zee") and the one related to low momentum electrons ("Electron LOWPT"). All the other uncertainties related to energy scale and resolution are summed in quadrature ("Electron E").

**Muons** The uncertainty on muon identification efficiency depends on the charge and momentum of the muon. Typically these uncertainties are of the order of a fraction of percent, and are referred as "Muon ID". The uncertainties on the muon energy scale and resolution are considered independently for the inner detector and muon spectrometer measurements, then are added in quadrature to eastimate the final effect ("Muon E").

**Taus** Hadronic tau object are only used in the analysis as a veto. Uncertainties on both tau energy scale and identification efficiency have been investigated and are found to be negligible for this analysis.

**Jets** The systematic uncertainties on the Jet Energy Scale (JES) are split up into multiple sets of nuisance parameters, which are related to different effects and components, for example the sensitivity to pileup or to the flavour composition of the jet. The overall uncertainty on the JES ranges between 3% and 7%, depending on the  $P_T$  and  $\eta$  of the jet. To give an idea of the effect that these uncertainty have on the analysis yield their sum in quadrature is reported in table 1.10 and 1.11 as "JES", however this is just a simplification for illustration purposes and in the limits extraction those uncertainties are considered uncorrelated. Systematic uncertainty

Source	b-tag category uncertainties (%)				
	Signal bbH	Signal ggH	$Z/\gamma^* \rightarrow \tau\tau$	Top	Other
Electron ID	2.3	2.6	2.8	1.8	2.0
Electron E	0.7	1.2	0.5	0.5	0.9
Electron LOWPT	0.4	0.0	0.4	0.1	0.4
Electron Zee	0.3	0.6	0.4	0.6	0.5
Muon ID	0.3	0.3	0.3	0.3	0.3
Muon E	0.5	0.8	0.1	0.1	0.2
Trigger Single Ele.	0.7	0.5	0.5	0.8	0.8
Trigger Dilepton	1.0	1.2	1.4	0.6	0.6
Embedding MFS	-	-	0.0	-	-
Embedding Iso.	-	-	1.3	-	-
JES	2.7	7.3	-	10.0	7.0
JER	1.4	6.3	-	2.9	3.0
B Eff	10.2	3.1	-	2.6	5.0
C Eff	0.2	4.3	-	0.0	1.2
L Eff	0.4	8.0	-	0.1	1.2
Pileup	0.4	0.7	0.4	0.4	0.9
MET	0.7	0.5	0.2	1.0	1.2
Luminosity	2.8	2.8	2.8	2.8	2.8

Table 1.10: Summary of the effect of the experimental systematic uncertainties on the yields of the different samples used in the b-tag channel. Here "Other" refers to the sum of all the remaining samples:  $W \rightarrow \ell\nu$ , diboson,  $Z \rightarrow \ell\ell$  and single top. The signal samples listed here are b-associated production and gluon fusion with  $m_A = 120$  GeV and  $\tan\beta = 20$ .

due to jet resolution ("Jet Resolution") are obtained by smearing the jet energy according to its uncertainty.

**b-Tagging** is described in chapter ???. Corrections are applied to simulation to match b-tagging efficiency in data, uncertainties on the knowledge of the b-tagging efficiencies for the 70% working point of the MV1 b-tagger are considered. The effect of those uncertainties is evaluated independently in the cases of b-quark, c-quark and light or gluon initiated jets and referred respectively to as "B Eff", "C Eff" and "L Eff". The tagging and mistagging efficiency uncertainties are considered to be totally anti-correlated.

**Missing Transverse Energy** The effect of the energy scale uncertainties for all the physics objects is propagated to the  $E_T^{miss}$  calculation. In addition uncertainty on the energy scale and resolution due to the remaining calorimeter energy deposit, the so called "soft-terms", are considered. All the uncertainty on  $E_T^{miss}$  are independently propagated through the analysis and are added in quadrature, this final term is referred as "MET" uncertainty.

Source	b-veto category uncertainties (%)				
	Signal bbH	Signal ggH	$Z/\gamma^* \rightarrow \tau\tau$	Top	Other
Electron ID	2.4	2.3	2.9 (s)	1.4	1.6
Electron E.	0.4	0.5	0.4	0.5	0.9
Electron LOWPT	0.3	0.5	0.4 (s)	0.0	1.2
Electron Zee	0.4	0.4	0.4 (s)	0.1	0.3
Muon ID	0.3	0.3	0.3	0.3	0.3
Muon E.	0.1	0.1	0.1	0.5	0.5
Trigger Single Ele.	0.6	0.6	0.5	0.9	0.9
Trigger Dilep.	1.0	1.0	1.3	0.2	0.3
Embedding MFS	-	-	0.1 (s)	-	-
Embedding Iso.	-	-	0.0 (s)	-	-
JES	0.6	0.7	-	1.0	1.2
JER	0.5	0.3	-	0.6	0.3
B Eff	1.8	0.0	-	12.0	0.8
C Eff	0.0	0.1	-	0.1	0.0
L Eff	0.0	0.1	-	0.2	0.1
Pileup	0.5	0.8	0.4	0.3	0.3
MET	0.2	0.8	0.1	0.2	0.5
Luminosity	2.8	2.8	2.8	2.8	2.8

Table 1.11: Summary of the effect of the experimental systematic uncertainties on the yields of the different samples used in the b-veto channel. Here "Other" refers to the sum of all the remaining samples:  $W \rightarrow \ell\nu$ , diboson,  $Z \rightarrow \ell\ell$  and single top. The signal samples listed here are b-associated production and gluon fusion with  $m_A = 120$  GeV and  $\tan\beta = 20$ . Shape uncertainty are noted with the symbol (s).

### 1.6.2 Theoretical Uncertainties

Uncertainties on the cross-sections that have been used to normalise simulation samples to data are reported in Table 1.13. These uncertainties include contributions due to parton distribution functions (PDFs), the choice of the value of strong coupling constant, and the renormalisation and factorisation scales. Furthermore the uncertainties on signal cross-section depends on  $\tan\beta$ , the Higgs boson type ( $A/h/H$ ) and mass.

The effect of systematic uncertainties due to various MC tuning parameters, underlying event and lepton kinematic description is considered. Since the effect on the invariant mass distribution of the di-tau system from these systematic uncertainties is negligible (as an example see Figure 1.13), only the variation in acceptance is considered as systematic uncertainty. The acceptance uncertainties for the ALPGEN Z MC, used for the normalisation of the embedded sample, are estimated at lepton preselection to be 4% [86]. Since additional selections are applied directly to the embedded sample, no further acceptance uncertainties is considered. Acceptance systematics on  $t\bar{t}$  simulated events are estimated to be of 2%. The acceptance uncertainties on diboson and single top production are assumed to be 2%. Uncertainties on signal acceptance have been estimated by producing samples with varied MC generator parameters and evaluating, at truth-level, the effect of analysis selections on leptons, taus and jets. This truth-level study is implemented within the Rivet framework [89], where additionally b-tagging is performed by identifying b-quarks and applying a weighting according to the estimated ATLAS b-tagging efficiencies [64]. The variation of the acceptance with respect to the nominal MC tune has been considered as a source of systematic uncertainty. For signal a total acceptance uncertainty varies from 4% to 30% depending on  $m_A$ , production process and on the analysis category.

### 1.6.3 $Z/\gamma^* \rightarrow \tau\tau$ Embedding Systematics

An important element of the embedding method is the subtraction of the calorimeter cells associated with the muons in the original  $Z \rightarrow \mu\mu$  event and their substitution with those from the simulated tau decays. To make a conservative estimate of the systematic uncertainty on this procedure, the energy of the subtracted cells is scaled up or down by 30%. The analysis is repeated with those modified samples and the relative uncertainty is referred as "EMB\_MFS", this uncertainty affects mainly the shape of the  $MMC_{mass}$  distribution, shown in figure 1.14.

In the selection of the  $Z \rightarrow \mu\mu$  sample only a loose requirement on muon track isolation is required. A different selection on the muon isolation may effect the selected sample by modifying the topology of the event, changing the non- $Z \rightarrow \mu\mu$  contamination or the activity in the calorimeter. To estimate the importance of these effects in our embedding sample, the isolation selection on the muons in the original  $Z \rightarrow \mu\mu$  events is tightened, a looser selection would have limited impact because of isolation requirements at trigger level. The resulting uncertainty, referred to as "EMB\_ISO", affects both the yield and the  $MMC_{mass}$  shape of the embedding samples, as shown in figure 1.14.

Finally, because the normalisation of the embedding sample is determined by the

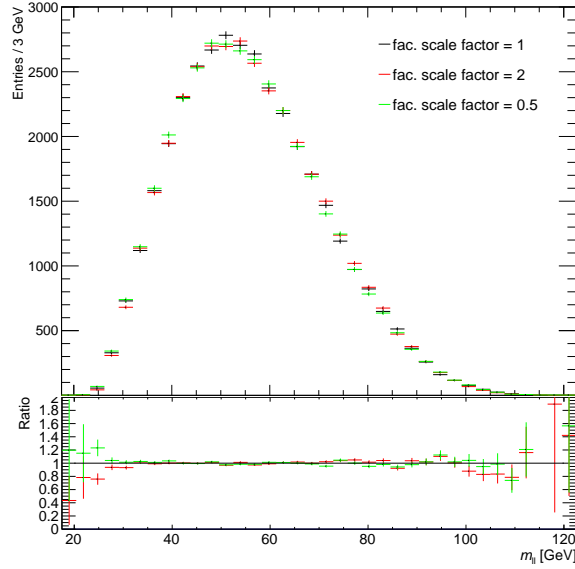


Figure 1.13: Comparison of the visible mass of tau decay products after factorisation scale variation for the b-veto category on a gluon fusion signal sample.

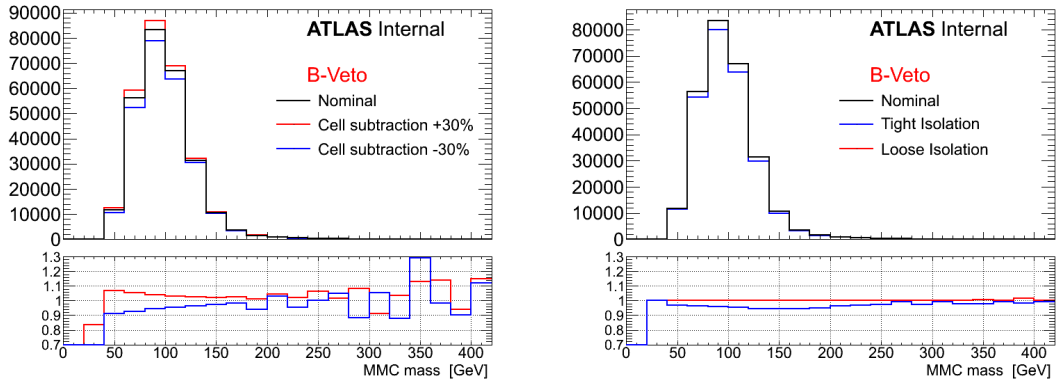


Figure 1.14: Impact of EMB\_MFS (left) and EMB\_ISO (right) systematic uncertainties on the  $MMC_{mass}$  distribution for Embedding sample. Only the b-veto category report significant deviations.

use of the ALPGEN sample, the relative cross section and luminosity uncertainties are assigned. In addition all the detector-related systematic uncertainties relevant to the decay products of the simulated tau decay are propagated to the embedding sample.

### 1.6.4 QCD Multi-Jet Systematics

In this analysis the QCD multi-jet background is estimated via the ABCD method, as described in Section 1.5.2. This technique relies strongly on the assumption that the lepton isolation variables are independent from the charge correlation between the two leptons. Systematic uncertainties are assigned to take into account deviations from this assumption. First the correlation between  $R_{QCD}$  and the lepton isolation selections is considered, then the result is compared with an auxiliary method.

Figure 1.15 shows the  $R_{QCD}$  factor, the ratio between the QCD yields in region C and D, as a function of the lepton isolation selections (red points). As described previously, the expectation from non-QCD backgrounds is subtracted from the data in regions C and D. To estimate the uncertainty on the value of  $R_{QCD}$  an additional transfer factor is defined as follows:  $R_{QCD}^{iso} = \hat{A}/\hat{B}$ , where  $\hat{A}$  and  $\hat{B}$  are semi-isolated OS and SS regions defined with the lepton isolation larger than the standard requirement, but less than a sliding cut. Once more, the non-QCD contributions are subtracted from the data yields. The regions  $\hat{A}$  and  $\hat{B}$  are chosen to be semi-isolated due to the high contamination of non-QCD background and possible signal in region A and B. Figure 1.15 shows  $R_{QCD}^{iso}$  as a function of the lepton isolation selections (black points). The difference between  $R_{QCD}$  and  $R_{QCD}^{iso}$  in the vicinity of the standard cut value is then assigned as a systematic uncertainty on  $R_{QCD}$ . Using the point where the cuts on the lepton isolation are twice their standard values, a systematic uncertainty of 15% is found. The plot in Figure 1.15 is made at preselection level, similar plots using the full selection for the two categories are in Appendix ??.

An additional method, used as a crosscheck, considers calculating  $R_{QCD}$  as the ratio between the estimated QCD contributions in region A and B. Here the non-QCD contributions are once more subtracted from data. However the large contribution of this non-QCD background, along with lack of statistics and possible signal contamination, lead to this method being only used as a cross check. Table 1.12 shows a comparison between  $R_{QCD}$  and  $R_{QCD}^{AB}$  for the two categories at the preselection stage of the cutflow, where signal contamination is negligible. Agreement is seen between  $R_{QCD}$  values in the two regions, within statistical uncertainties.

The difference in  $MMC_{mass}$  shape observed between the OS and SS anti-isolated regions (C and D) is shown in Figure 1.16. This effect is within the uncertainty on  $R_{QCD}$  of the ABCD method, hence no correction factor is applied to the mass shape. We assume, however, that there could be the same shape difference in the isolated regions, a shape uncertainty is then assigned to region B to take into account this deviation. Further shape uncertainties due to non-QCD background subtraction are found to be negligible. The uncertainty due to the use of an isolation requirement at trigger level is discussed in Appendix ?? and is found to be negligible.

Selection	$R_{QCD}$	$R_{QCD}^{AB}$	$R_{QCD}^{iso}$
Preselection	$1.929 \pm 0.004$	$2.12 \pm 0.17$	$2.22 \pm 0.16$
B-veto	$1.965 \pm 0.005$	$2.10 \pm 0.16$	$2.22 \pm 0.16$
B-tag	$1.78 \pm 0.02$	$1.9 \pm 0.9$	$2.0 \pm 0.8$

Table 1.12: Comparison between  $R_{QCD}$ ,  $R_{QCD}^{AB}$  and  $R_{QCD}^{iso}$  for early stage in the cutflow, only b-tag and b-veto requirement are applied after preselections. Reported is statistical uncertainty only.

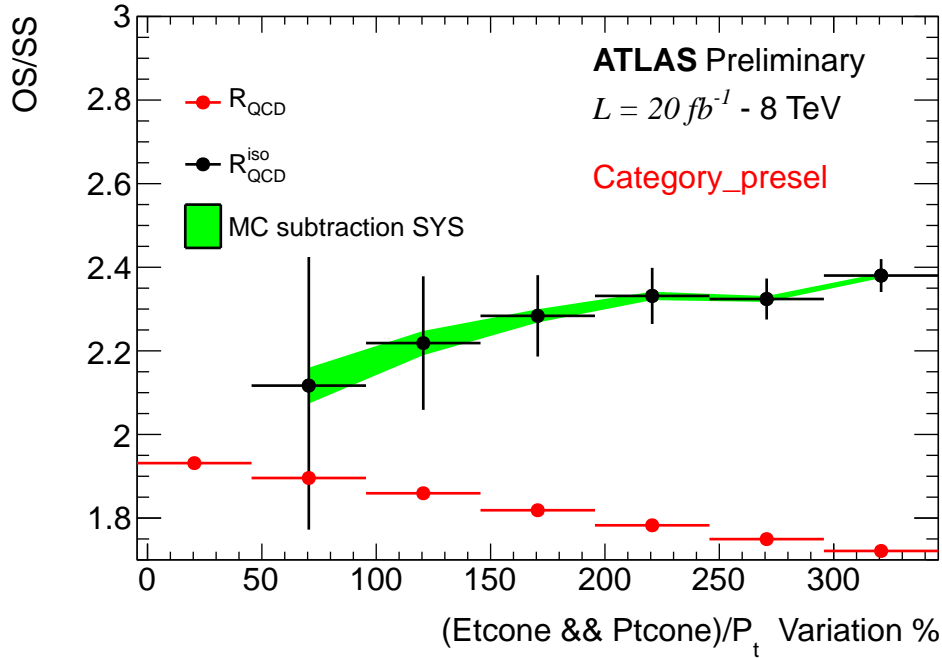


Figure 1.15: OS/SS ratio as a function of lepton isolation variable selections. The selections are varied as a percentage relative to the standard lepton isolation cut values (0 in the plot). The red points show the anti-isolated scale factor  $R_{QCD}$ , i.e. the ratio between regions C and D. The black points show the isolated scale factor, which is defined as the ratio between region  $\hat{A}$  and  $\hat{B}$ , where the leptons have isolation values larger than the nominal value but smaller than the sliding cut on X axis.

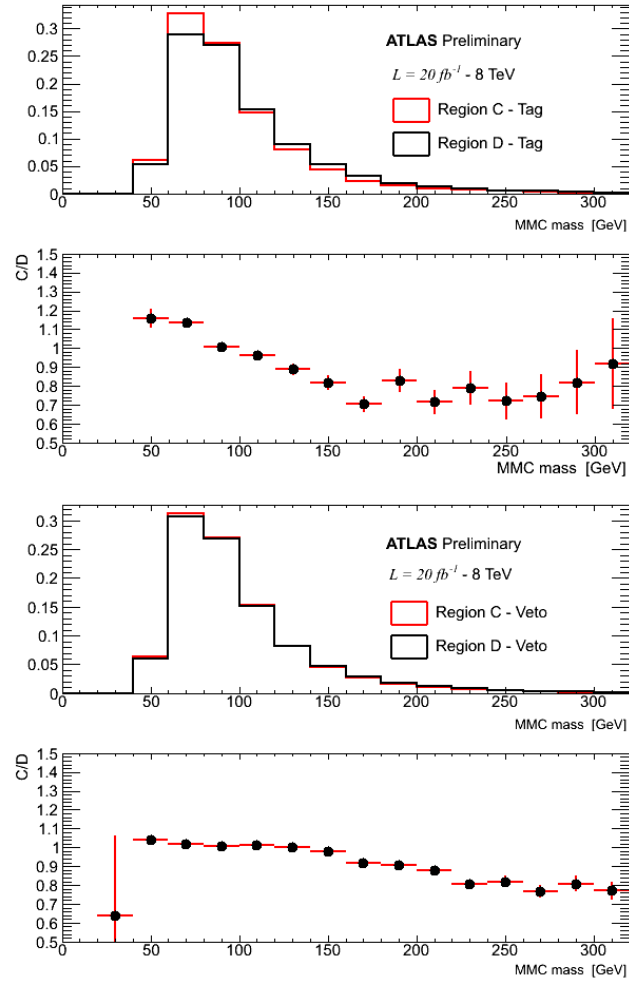


Figure 1.16: Shape differences for the b-tag and b-veto categories between the ABCD regions C and D.



Generator	Process	Uncertainty
ALPGEN	$Z \rightarrow \tau\tau/ee/\mu\mu$	$\pm 5\%$
POWHEG	$t\bar{t}$	$\pm 5.5\%$
ALPGEN	$W \rightarrow \tau\nu/e\nu/\mu\nu$	$\pm 5\%$
AcerMC	single top	$\pm 13\%$
HERWIG	dibosons	$\pm 6\%$
SHERPA	$bbA/h/H$ ( $m_A \geq 120$ GeV)	$-( < 20 )\%, +( < 9 ) \%$
SHERPA	$bbA/h/H$ ( $m_A = 110$ GeV)	$-( < 25 )\%, +( < 9 ) \%$
SHERPA	$bbA/h/H$ ( $m_A = 100$ GeV)	$-( < 28 )\%, +( < 9 ) \%$
SHERPA	$bbA/h/H$ ( $m_A = 90$ GeV)	$-( < 30 )\%, +( < 9 ) \%$
POWHEG	$ggA/h/H$ ( $m_A \leq 300$ GeV)	$< 15\%$

Table 1.13: Cross-section uncertainties for background and signal samples. The reported signal samples are all for  $\tan\beta = 20$ .

## 1.7 Results

### 1.7.1 LHC Procedure For Limits Setting

A detailed description of the LHC procedure for Higgs search can be found in [?, ?], in the following a brief summary is given. Statistical tests are used to quantify an observation or to set an exclusion limit, in search for new phenomena, hypothesis testing is performed by means of two hypotheses: the *background only*  $H_0$  and the *signal+background*  $H_1$ . As it has already been outlined in section ??, any statistical test is based on probability distribution, once a probability density function (p.d.f.) is defined, one can calculate its value for a given set of data obtaining what is called a "likelihood". Taking the marked Poisson p.d.f. in equation (??) one obtains the following likelihood function:

$$\mathcal{L}(\text{data}|\mu, \boldsymbol{\theta}) = \text{Poisson}(\text{data}|\mu \cdot s(\boldsymbol{\theta}) + b(\boldsymbol{\theta})) \cdot f(\boldsymbol{\theta}|\hat{\boldsymbol{\theta}}) \quad (1.3)$$

this now describes how likely are the data under a certain hypothesis and it is only a function of the parameter  $\mu$  and of the nuisance parameter  $\boldsymbol{\theta}$ . If the hypothesis under test is unlikely to happen with the given dataset the value of  $\mathcal{L}$  is decreasing, one can define which is the best value of a parameter that describes the data via maximising the likelihood, obtaining a so called maximum likelihood estimator. The Poisson distribution in equation (1.3) stands for a product of Poisson probabilities to observe events in the bin  $i$  of an histogram:

$$\prod_i \frac{(\mu s_i + b_i)^{n_i}}{n_i!} e^{-\mu s_i - b_i}$$

while the  $f(\boldsymbol{\theta}|\hat{\boldsymbol{\theta}})$  is the p.d.f. for a given set of nuisance parameter  $\boldsymbol{\theta}$  with their best estimate  $\hat{\boldsymbol{\theta}}$ .

To compute the compatibility of the data with the  $H_0$  and  $H_1$  hypothesis and then exclusion limits, one needs to define a test statistic. The test statistic, which has already been mentioned in section ??, is a function of the data which returns a

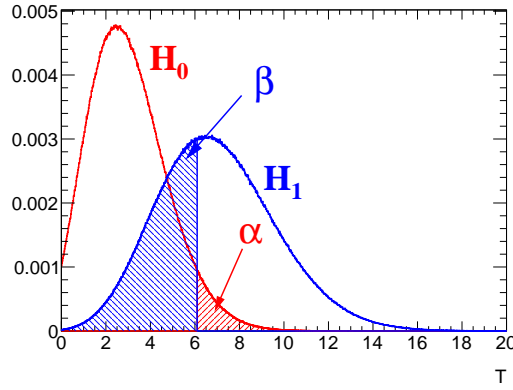


Figure 1.17: Example of a test statistic which in this case is just the total number of events of a counting experiment. Under the hypothesis  $H_0$  are expected four events, while under the  $H_1$  seven events are expected.

real value. One can in principle use any test statistic, however, given the size of the test (probability to reject the null hypothesis when is true) one would like to have a test statistic which has the highest power  $1 - \beta$  possible (probability to reject the null hypothesis when it is false). Figure 1.17 shows an example of the distribution of an hypothetical test statistic for two hypothesis. It has been shown by Neuman-P [1] that in case of simple hypothesis (probability model without any parameter), then the test statistic with the highest power is the ratio of the likelihood calculated with the two hypothesis. The standard procedure at the LHC is to use the following test statistic [2] based on the likelihood ratio:

$$\tilde{q}_\mu = -2 \ln \frac{\mathcal{L}(\text{data}|\mu, \hat{\theta}_\mu)}{\mathcal{L}(\text{data}|\hat{\mu}, \hat{\theta})} \quad \text{with the constraint} \quad 0 \leq \hat{\mu} \leq \mu$$

where  $\hat{\mu}$  and  $\hat{\theta}$  are the maximum likelihood estimators for  $\mu$  and  $\theta$  given the data, whereas  $\hat{\theta}_\mu$  is the maximum likelihood estimator of  $\theta$  given the data but considering a signal strength of value  $\mu$ ,  $\tilde{q}_\mu$  is increasing with increasing disagreement between data and the  $\mu$  hypothesis under test. The procedure for limits setting follows five steps:

1. The signal hypothesis with signal strength  $\mu$  is assumed, under this assumption a set of *pseudo-data* is generated for different values of  $\mu$ .
2.  $\tilde{q}_\mu$  is calculated for each of the *pseudo-dataset* and each signal hypothesis generating the expected probability density function for  $\tilde{q}_\mu$  given  $\mu$ ,  $f(\tilde{q}_\mu | \mu, \hat{\theta}_\mu, H_1)$ .
3. One does the same thing for the null hypothesis, generate pseudo-data with the distribution of background only and obtain the  $f(\tilde{q}_\mu | \mu = 0, \hat{\theta}_0, H_0)$ .
4. Once the p.d.f. for the signal and signal + background hypothesis is obtained, one can define for a given dataset (that can be this time real data or again pseudodata) two p-values for any given value of  $\mu$ , which are the probability

to obtain data less compatible with the hypotesis in consideration:

$$p_{s+b} = P(\tilde{q}_\mu > \tilde{q}_\mu^{observed} \mid H_1)$$

$$p_b = P(\tilde{q}_\mu > \tilde{q}_\mu^{observed} \mid H_0)$$

The ratio of this two probability is what is called the  $CL_s = p_{s+b}/p_b$  [].

5. If for a given  $\mu$  is obtained  $CL_s \leq \alpha$  one states that the signal hypotesis (with that  $\mu$ ) is excluded with  $(1 - \alpha)$   $CL_s$  confidence level. To get the 95% confidence level upper limit on  $\mu$ , denoted as  $\mu^{95}$  one adjust  $\mu$  until  $CL_s = 0.05$ .

This is a quite complicated prescription, however its interpretation is not so different from the usual Neyman Costruction [] of confidence intervals: for each  $\mu$  is possible to define  $\tilde{q}_\mu^{95}$  for which the probability  $P(\tilde{q}_\mu \geq \tilde{q}_\mu^{95} \mid \mu, H_1) = 5\%$ , this means that if  $H_1$  is true one expects  $\tilde{q}_\mu \geq \tilde{q}_\mu^{95}$  in 5% of the cases. With this definition  $\mu^{95}$  would be the value of  $\mu$  that for the observed data gives  $\tilde{q}_\mu = \tilde{q}_\mu^{95}$ , or in other words a p-value of 5%. By costruction, rejecting  $\mu > \mu^{95}$  the hypotesis  $H_1$  will be rejected, when is true, at most 5% of the time, given the fact that  $\tilde{q}_\mu$  is increasing with increasing discrepancy of the hypotesis with data. The difference with the  $CL_s$  prescription is that there the ratio of p-values is used to define  $\mu^{95}$ : it has been shown that this choice protect the upper limit from down fluctuation of the data, giving a conservative estimate in any case.

The expected median exclusion upper-limit and its error are evaluated by generating a large sample of *background only* pseudo-data and calculating  $CL_s$  and  $\mu^{95}$  for each of them, from the distribution of  $\mu^{95}$  one can get the mean excluded value and its error.

The actual implementation in the limit framework of the ABCD method follows that suggested in [84]. Here three free parameters are fitted: number of multi-jet events in region B,  $N_B^{QCD}$ , factor that extrapolates from SS region to OS regions,  $R_{QCD}$ , and the factor that extrapolates from isolated to anti-isolated regions  $R_{BD}$ . Neglecting signal contributions, the following equations can be written for the event yield of the B,C and D control regions:

$$N_B = N_B^{BKG} + N_B^{QCD}$$

$$N_C = N_C^{BKG} + N_B^{QCD} \times R_{QCD} \times R_{BD}$$

$$N_D = N_D^{BKG} + N_B^{QCD} \times R_{BD}$$

where  $N^{BKG}$  represent the prediction of non-QCD background in the relative regions. The estimate of multi-jet event yield in SR will be then  $N_B^{QCD} \times R_{QCD}$ . This method is particularly powerful because in the best fit of  $R_{QCD}$  the statistical and systematics uncertainty for non-QCD backgrounds and data will be considered.

Sample	b-tag category			b-veto category		
	N(event)	Stat.	Syst.	N(event)	Stat.	Syst.
$Z/\gamma^* \rightarrow \tau\tau$	418	$\pm 6$		54680	$\pm 60$	
$t\bar{t}$	330	$\pm 10$		2228	$\pm 25$	
Multijet	100	$\pm 15$		3940	$\pm 330$	
$W \rightarrow \ell\nu$	10	$\pm 6$		650	$\pm 100$	
Diboson	13.1	$\pm 1.8$		2921	$\pm 27$	
Single Top	90	$\pm 6$		443	$\pm 15$	
$Z \rightarrow \ell\ell$	0.9	$\pm 0.8$		430	$\pm 40$	
Total	962	$\pm 16$		65290	$\pm 180$	
Signal						
Data	-	-	-	-	-	-

Table 1.14: Comparison between yield in data and the one expected from our background model, b-tag and b-veto category are reported separately.

### 1.7.2 Exclusion Limits

The procedure described in section 1.7.1 is the one used for the SM Higgs, for the MSSM further complication arises: one has to consider in the signal model three Higgses, in a particular scenario the masses and cross section are defined for a given point in the  $\tan\beta - m_A$  plane, so the procedure described previously has to be repeated for each point in that plane. For the  $m_h^{max}$  scenario exclusion limits are derived by calculating 95% CLs limits on the cross section of  $bb/gg \rightarrow A/H/h \rightarrow \tau_{lep}\tau_{lep}$  for 15  $\tan\beta$  values (between<sup>3</sup>  $\tan\beta = 5$  and  $\tan\beta = 60$ ), a point in the  $\tan\beta - m_A$  plane is excluded if  $\mu^{95} \leq 1$  for that point, a linear interpolation is used to determine the  $\tan\beta$  excluded for a given  $m_A$ . The procedure is followed for a set of different CP-odd Higgs masses  $m_A$ : 90, 100, 110, 120, 125, 130, 140, 150, 170, 200, 250 and 300 GeV. The event yield has been compared between data and background expectation in bins of the  $MMC_{mass}$  distribution. The bin sizes were chosen such that there are enough events left for the asymptotic approximation [90] to hold. Table 1.14 compares yields between data and background model for the two categories at the final stage of the cut flow. Additionally, figure 1.18 shows the  $MMC_{mass}$  distributions for the full b-tag and b-veto categories.

The resulting exclusion limit on the MSSM parameter space ( $m_A$  vs  $\tan\beta$  plane) are interpreted within the  $m_h^{max}$  benchmark scenario [28] and shown in Figure 1.19. The expected and observed 95% confidence-level limits are shown as solid and dashed black lines, the green and yellow bands correspond to the  $1\sigma$  and  $2\sigma$  error bands. The analysis is sensitive to MSSM Higgs production of  $\tan\beta \geq 13$  for the range  $90 < m_A < 200$  GeV. The observed limit is presently unknown.

The outcome of the search is also interpreted in the generic case of a scalar boson produced in the  $pp \rightarrow gg \rightarrow \phi$  or  $pp \rightarrow bb\phi$  mode and decaying to a di-tau pair. These limits are shown in Figure 1.20 for the b-associated and the gluon-gluon

<sup>3</sup>The set of  $\tan\beta$  values used is 5, 8, 10, 13, 16, 20, 23, 26, 30, 35, 40, 45, 50, 55, 60

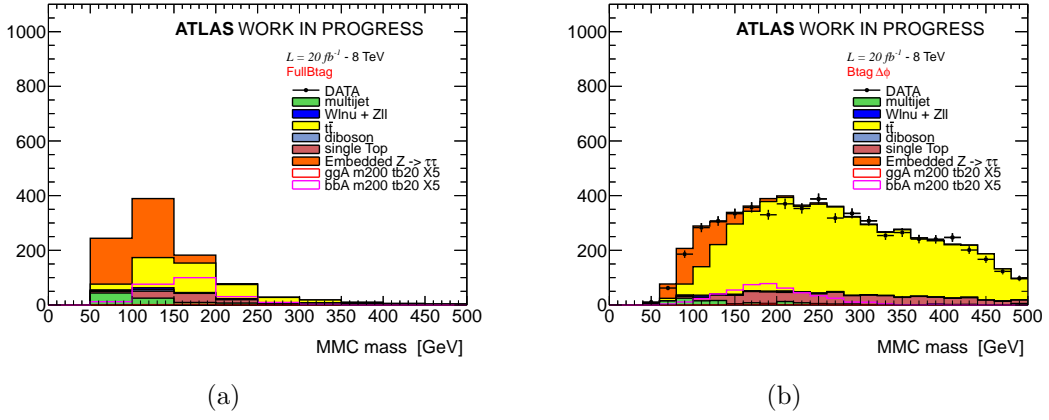


Figure 1.18: Distributions of the  $MMC_{mass}$  mass for (a) the full b-tag category selection and (b) the full b-veto selection.

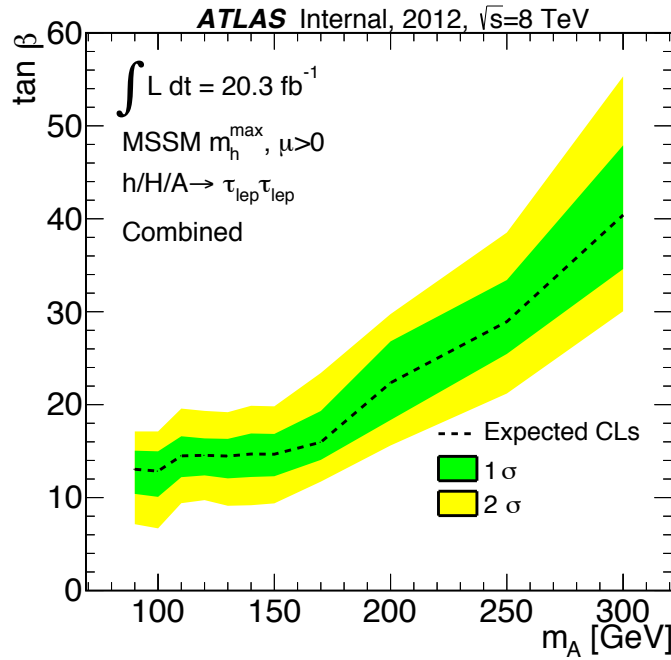


Figure 1.19: Expected exclusion limits for MSSM Higgs boson production in the MSSM  $m_A$  vs  $\tan \beta$  parameter space. Combination between b-tag and b-veto category.

Figure 1.20: Limits on the production of a scalar particle decaying to a di-tau pair and produced in association with b quarks (left) or via gluon-gluon fusion (right). Still not produced...

fusion production mechanisms separately. All signal systematic uncertainties are implemented in the likelihood for this limit derivation, more information about the limits and their validation can be found in Appendix ??.

# Bibliography

- [1] L. Evans and P. Bryant, *LHC Machine*, JINST **3** (2008) S08001.
- [2] F. Englert and R. Brout, *Broken Symmetry and the Mass of Gauge Vector Mesons*, Phys. Rev. Lett. **13** (1964) 321.
- [3] P. W. Higgs, *Broken symmetries, massless particles and gauge fields*, Phys. Lett. **12** (1964) 132.
- [4] P. W. Higgs, *Broken Symmetries and the Masses of Gauge Bosons*, Phys. Rev. Lett. **13** (1964) 508.
- [5] P. W. Higgs, *Spontaneous Symmetry Breakdown without Massless Bosons*, Phys. Rev. **145** (1966) 1156.
- [6] G. S. Guralnik, C.R. Hagen and T. W. B. Kibble Phys.Rev.Lett. **13** (1964) 585.
- [7] N. P. Nilles, *Supersymmetry, supergravity and particle physics*, Phys. Rep. **110** (1984) 1.
- [8] H. E. Haber and G. L. Kane, *The search for supersymmetry: Probing physics beyond the standard model*, Phys. Rep. **117** (1985) 75.
- [9] ALEPH, DELPHI, L3 and OPAL Collaboration, *Search for neutral MSSM Higgs bosons at LEP*, Eur. Phys. J. **C47** (2006) 547.
- [10] *Combined CDF and D0 upper limits on MSSM Higgs boson production in tau-tau final states with up to  $2.2 \text{ fb}^{-1}$  of data*, arXiv:1003.3363 [hep-ex].
- [11] The CMS Collaboration, S. Chatrchyan et al., arXiv:1104.1619 [hep-ex] [hep-ex].
- [12] The ATLAS Collaboration, *Search for the neutral Higgs bosons of the Minimal Supersymmetric Standard Model in  $pp$  collisions at  $\sqrt{s} = 7 \text{ TeV}$  with the ATLAS detector*, arXiv:1211.6956 [hep-ex].
- [13] S. Heinemeyer, O. Stål and G. Weiglein, *Interpreting the LHC Higgs search results in the MSSM*, Phys.Lett. **B710** (2012) 201–206, arXiv:1112.3026 [hep-ph].

- [14] A. Arbey, M. Battaglia, A. Djouadi and F. Mahmoudi, *The Higgs sector of the phenomenological MSSM in the light of the Higgs boson discovery*, JHEP **1209** (2012) 107, [arXiv:1207.1348 \[hep-ph\]](#).
- [15] The ATLAS Collaboration, G. Aad et al., *The ATLAS Experiment at the CERN Large Hadron Collider*, JINST **3** (2008) S08003.
- [16] M. L. Mangano et al., *ALPGEN, a generator for hard multiparton processes in hadronic collisions*, JHEP **07** (2003) 001.
- [17] J. Alwall et al., *Comparative study of various algorithms for the merging of parton showers and matrix elements in hadronic collisions*, Eur. Phys. J. **C53** (2008) 473, [arXiv:0706.2569](#).
- [18] S. Frixione and B. R. Webber, *Matching NLO QCD computations and parton shower simulations*, JHEP **06** (2002) 029, [hep-ph/0204244](#).
- [19] B. P. Kersevan and E. Richter-Was, *The Monte Carlo Event Generator AcerMC 2.0 with Interfaces to PYTHIA 6.2 and HERWIG 6.5*, [arXiv:0405247v1 \[hep-ph\]](#).
- [20] G. Corcella et al., *HERWIG 6: an event generator for hadron emission reactions with interfering gluons (including supersymmetric processes)*, JHEP **01** (2001) 010.
- [21] J. M. Butterworth, J. R. Forshaw, and M. H. Seymour, *Multiparton Interactions in Photoproduction at HERA*, Z. Phys. **C72** (1996) 637.
- [22] T. Binoth, M. Ciccolini, N. Kauer, and M. Kramer, *Gluon-induced W-boson pair production at the LHC*, JHEP **12** (2006) 046.
- [23] A. S. et al., *Higgs boson production in gluon fusion*, JHEP **02** (2009) 029.
- [24] T. Gleisberg et al., *Event generation with SHERPA 1.1*, JHEP **02** (2009) 007.
- [25] J. Pumplin, D. R. Stump, J. Huston, H. L. Lai, P. M. Nadolsky and W. K. Tung, “New generation of parton distributions with uncertainties from global QCD analysis,” JHEP **0207** (2002) 012 [[hep-ph/0201195](#)].
- [26] H. -L. Lai, M. Guzzi, J. Huston, Z. Li, P. M. Nadolsky, J. Pumplin and C. -P. Yuan, “New parton distributions for collider physics,” Phys. Rev. D **82** (2010) 074024 [[arXiv:1007.2241 \[hep-ph\]](#)].
- [27] S. Heinemeyer *et al.* [LHC Higgs Cross Section Working Group Collaboration], “Handbook of LHC Higgs Cross Sections: 3. Higgs Properties,” [arXiv:1307.1347 \[hep-ph\]](#).
- [28] M. Carena, S. Heinemeyer, C. E. M. Wagner, and G. Weiglein, *Suggestions for benchmark scenarios for MSSM Higgs boson searches at hadron colliders*, Eur. Phys. J. **C26** (2003) 601–607, [hep-ph/0202167](#).



- [29] The ATLAS Collaboration, *ATLAS Monte Carlo Tunes for MC09*, ATL-PHYS-PUB-2010-002.
- [30] S. Jadach, J. H. Kuhn and Z. Was, *TAUOLA - a library of Monte Carlo programs to simulate decays of polarized  $\tau$  leptons*, Comput. Phys. Commun. **64** (1990) 275.
- [31] E. Barberio, B. V. Eijk and Z. Was, *Photos - a universal Monte Carlo for QED radiative corrections in decays*, Comput. Phys. Commun. **66** (1991) 115.
- [32] The GEANT4 Collaboration, S. Agostinelli et al., *GEANT4 - a simulation toolkit*, Nucl. Instrum. Meth. **A506** (2003) 250.
- [33] The ATLAS Collaboration, G. Aad et al., *The ATLAS Simulation Infrastructure*, ATLAS-SOFT-2010-01-004, submitted to Eur. Phys. J. C., [arXiv:1005.4568](#).
- [34] The ATLAS Collaboration, *Estimation of  $Z/\gamma^* \rightarrow \tau\tau$  Background in VBF  $H \rightarrow \tau\tau$  Searches from  $Z \rightarrow \mu\mu$  Data using an Embedding Technique*, ATL-PHYS-INT-2009-109.
- [35] The ATLAS Collaboration, *Search for the Standard Model Higgs boson in the  $H \rightarrow \tau\tau$  decay mode with  $4.7\text{ fb}^{-1}$  of ATLAS detector*, Tech. Rep. ATLAS-CONF-2012-014, CERN, Geneva, Mar, 2012.
- [36] The ATLAS Collaboration, *Search for the Standard Model Higgs boson  $H \rightarrow \tau\tau$  decays with the ATLAS detector*, ATL-COM-PHYS-2013-722.
- [37] T. S. et al., *Z physics at LEP 1*, CERN 89-08 **3** (1989) 143.
- [38] The ATLAS Collaboration, Inner Detector: Technical Design Report, CERN/LHCC/97-016/017 (1997).
- [39] The ATLAS Collaboration, G. Aad et al., The ATLAS Experiment at the CERN Large Hardon Collider, 2008 JINST 3 S08003.
- [40] A. Bazan, T. Bouedo, P. Ghez, M. Marino and C. Tull, "The Athena data dictionary and description language," eConf C **0303241** (2003) MOJT010 [cs/0305049 [cs-se]].
- [41] The ATLAS Collaboration, *Expected Performance of the ATLAS Experiment - Detector, Trigger and Physics*, CERN-OPEN-2008-020, [arXiv:0901.0512](#).
- [42] T. Cornelissen et al., Concepts, Design and Implementation of the ATLAS New Tracking, ATLAS Note ATL-SOFT-PUB-2007-007 (2007).
- [43] Kalman, R. E. (1960). "A New Approach to Linear Filtering and Prediction Problems". Journal of Basic Engineering 82 (1): 3545. doi:10.1115/1.3662552
- [44] The ATLAS Collaboration, Performance of primary vertex reconstruction in proton-proton collisions at  $s = \sqrt{s}(7)$  TeV in the ATLAS experiment. ATLAS-CONF-2010-069.

- [45] R. Fruhwirth, W. Waltenberger, P. Vanlaer, *Adaptive vertex fitting*, J. Phys. G34 (2007).
- [46] The ATLAS Collaboration, *Characterization of Interaction-Point Beam Parameters Using the pp Event-Vertex Distribution Reconstructed in the ATLAS Detector at the LHC*, ATL-CONF-2010-027.
- [47] The ATLAS collaboration, *Expected electron performance in the ATLAS experiment*, ATL-PHYS-PUB-2011-006
- [48] The ATLAS Collaboration, *Electron reconstruction and identification efficiency measurements with the ATLAS detector using the 2011 LHC proton-proton collision data*, CERN-PH-EP-2014-040, arXiv:1404.2240
- [49] The ATLAS Collaboration, G. Aad et al., *Electron performance measurements with the ATLAS detector using the 2010 LHC proton-proton collision data*, Eur.Phys.J. C72 (2012) 1909.
- [50] S. Hassini, et al., *A muon identification and combined reconstruction procedure for the ATLAS detector at the LHC using the (MUONBOY, STACO, MuTag) reconstruction packages*, NIM A572 (2007) 7779.
- [51] The ATLAS Collaboration, G. Aad et al., *Preliminary results on the muon reconstruction efficiency, momentum resolution, and momentum scale in ATLAS 2012 pp collision data*, ATLAS-CONF-2013-088, CERN, 2013,
- [52] M. Cacciari, G. P. Salam, and G. Soyez, *FastJet user manual*, Eur.Phys.J. C72 (2012) 1896.
- [53] W. Lampl et al., *Calorimeter Clustering Algorithms : Description and Performance*, ATL-LARG-PUB-2008-002.
- [54] M. Cacciari, G. P. Salam, and G. Soyez, *The anti-kt jet clustering algorithm*, JHEP 04 (2008) 63.
- [55] E. Abat, J. Abdallah, T. Addy, P. Adragna, et al., *Combined performance studies for electrons at the 2004 ATLAS combined test-beam*, JINST 5 (2010) P11006.
- [56] ATLAS Collaboration, *Jet energy measurement with the ATLAS detector in proton-proton collisions at  $\sqrt{s} = 7$  TeV*, Submitted to EPJ (2011) , arXiv:1112.6426
- [57] The ATLAS Collaboration, *Pile-up corrections for jets from proton-proton collisions at ATLAS in 2011*, ATLAS-CONF-2012-064, July, 2012.
- [58] M. Cacciari and G. P. Salam, *Pileup subtraction using jet areas*, Phys.Lett. B659 (2008) 119.

- [59] The ATLAS Collaboration, G. Aad et al., *Jet energy resolution in proton-proton collisions at  $\sqrt{s} = 7$  TeV recorded in 2010 with the ATLAS detector*, Eur.Phys.J. C73 (2013) 2306
- [60] The ATLAS collaboration, *Jet energy scale and its systematic uncertainty in proton-proton collisions at  $\sqrt{s} = 7$  TeV with ATLAS 2011 data*, ATLAS-CONF-2013-004
- [61] The ATLAS Collaboration, *Data-Quality Requirements and Event Cleaning for Jets and Missing Transverse Energy Reconstruction with the ATLAS Detector in Proton-Proton Collisions at a Center-of-Mass Energy of  $\sqrt{s} = 7$  TeV*, ATLAS-CONF-2010-038.
- [62] G. Piacquadio, C. Weiser, *A new inclusive secondary vertex algorithm for b-jet tagging in ATLAS*, JPCS 119 (2008) 032032
- [63] The ATLAS Collaboration, G. Aad et al., *Commissioning of the ATLAS high-performance b-tagging algorithms in the 7 TeV collision data*, ATLAS-CONF-2011-102, CERN, 2011, ATLAS-CONF-2011-102.
- [64] The ATLAS Collaboration, *Measuring the b-tag efficiency in a  $t\bar{t}$  sample with  $4.7 \text{ fb}^{-1}$  of data from the ATLAS detector* ATLAS-CONF-2012-097.
- [65] The ATLAS Collaboration, *Calibration of b-tagging using dileptonic top pair events in a combinatorial likelihood approach with the ATLAS experiment* ATLAS-CONF-2014-004.
- [66] The ATLAS Collaboration, *Reconstruction and Calibration of Missing Transverse Energy and Performance in Z and W events in ATLAS Proton-Proton Collisions at  $\sqrt{s}=7$  TeV*, ATLAS-CONF-2011-080.
- [67] ATLAS Collaboration, G. Aad et al., *Performance of missing transverse momentum reconstruction in proton-proton collisions at 7 TeV with ATLAS*, Eur.Phys.J. C72 (2012) 1844.
- [68] TheATLAS Collaboration, *Performance of the Reconstruction and Identification of Hadronic tau Decays in ATLAS with 2011 Data*, ATLAS-CONF-2012-142.
- [69] The ATLAS Collaboration, G. Aad et al., *Performance of the ATLAS trigger system in 2010*, Eur.Phys.J. C72 (2012) 1849.
- [70] The ATLAS Collaboration, G. Aad et al., *Performance of the ATLAS muon trigger in 2011*, ATLAS-CONF-2012-099, CERN, 2012.
- [71] The ATLAS Collaboration, G. Aad et al., *Performance of the ATLAS electron and photon trigger in p-p collisions at  $\sqrt{s} = 7$  TeV in 2011*, ATLAS-CONF-2012-048, CERN, 2012.
- [72] M. Dobbs and J.B. Hansen, *The HepMC C++ Monte Carlo Event Record for High Energy Physics*, Computer Physics Communications, ATL-SOFT-2000-001.

- [73] The ATLAS Collaboration, *Observation of a new particle in the search for the Standard Model Higgs boson with the ATLAS detector at the LHC*, Physics Letters B **716** (2012) 1–29.
- [74] The CMS Collatoration, *Observation of a new boson at a mass of 125 GeV with the CMS experiment at the LHC*, Physics Letters B **716** (2012) 30–61.
- [75] The ATLAS Collaboration, *Evidence for the spin-0 nature of the Higgs boson using ATLAS data*, Phys. Lett. B **726** (2013), pp. 120-144.
- [76] The ATLAS Collaboration, *Measurements of Higgs boson production and couplings in diboson final states with the ATLAS detector at the LHC*, Phys. Lett. B **726** (2013), pp. 88-119.
- [77] The CMS Collaboration, “*Evidence for the direct decay of the 125 GeV Higgs boson to fermions*,” arXiv:1401.6527 [hep-ex].
- [78] The CMS Collaboration, *Higgs boson width from on- vs. off-shell production and decay to Z-boson pairs*, arXiv:1405.3455.
- [79] A. Elagin, P. Murat, A. Pranko, and A. Safonov, *A New Mass Reconstruction Technique for Resonances Decaying to di-tau*, arXiv:1012.4686 [hep-ex]. \* Temporary entry \*.
- [80] T. A. Collaboration, *Search for neutral MSSM Higgs bosons decaying to  $\tau\tau$  pairs in proton-proton collisions at with the ATLAS detector*, Physics Letters B **705** (2011) no. 3, 174 – 192.
- [81] The ATLAS Collaboration, *Data-driven estimation of the background to charged Higgs boson searches using hadronically-decaying tau final states in ATLAS*, ATLAS-CONF-2011-051.
- [82] The ATLAS Collaboration, *Measurement of the  $Z \rightarrow \tau\tau$  cross section with the ATLAS detector*, Phys. Rev. D **84** (2011) 112006.
- [83] T. A. Collaboration, *Search for the neutral Higgs bosons of the Minimal Supersymmetric Standard Model in pp collisions at  $\sqrt{s} = 7$  TeV with the ATLAS detector*, JHEP, arXiv:1211.6956.
- [84] Atlas statistics forum, *ABCD method in searches*, link
- [85] The ATLAS Collaboration, *Search for Neutral MSSM Higgs Bosons  $H$  to  $\tau\tau$  to  $l\tau_h$  with the ATLAS Detector in 7 TeV Collisions*, ATL-COM-PHYS-2012-094.
- [86] The ATLAS Collaboration, *Search for neutral Higgs Bosons in the decay mode  $H \rightarrow \tau\tau \rightarrow ll+4\nu$  in proton proton collision at  $\sqrt{7}$  TeV with the ATLAS Detector*, ATL-COM-PHYS-2011-758.
- [87] The ATLAS Collaboration, *Luminosity Determination in pp Collisions at  $\sqrt{s} = 7$  TeV using the ATLAS Detector in 2011*, ATLAS-CONF-2011-116.

- [88] T. Sjostrand, S. Mrenna and P. Skands, *PYTHIA 6.4 physics and manual*, JHEP **05** (2006) 026.
- [89] A. B. et al., *Rivet user manual*, arXiv:1003.0694 [hep-ph].
- [90] E. G. G. Cowan, K. Cranmer and O. Vitells, *Asymptotic formulae for likelihood-based tests of new physics*, arXiv:1007.1727 [hep-ex].
- [91] LHC Higgs Cross Section Working Group, S. Dittmaier, C. Mariotti, G. Passarino, R. Tanaka (Eds.), et al., *Handbook of LHC Higgs Cross Sections: 1. Inclusive Observables*, arXiv:1101.0593 [hep-ph].
- [92] LHC Higgs Cross Section Working Group, S. Dittmaier, C. Mariotti, G. Passarino, and R. Tanaka (Eds.), *Handbook of LHC Higgs Cross Sections: 2. Differential Distributions*, CERN-2012-002 (CERN, Geneva, 2012) , arXiv:1201.3084 [hep-ph].
- [93] ATLAS collaboration *Performance of the ATLAS Silicon Pattern Recognition Algorithm in Data and Simulation at  $\sqrt{s} = 7$  TeV*, ATLAS-CONF-2010-072
- [94] The ATLAS Collaboration, *A measurement of the material in the ATLAS inner detector using secondary hadronic interactions*, arXiv:1110.6191, JINST 7 (2012) P01013
- [95] The ATLAS Collaboration, *Validation of the ATLAS jet energy scale uncertainties using tracks in proton-proton collision  $\sqrt{s} = 7$  TeV*, ATLAS-CONF-2011-067
- [96] The ATLAS Collaboration, *Track Reconstruction Efficiency in  $\sqrt{s} = 7$  TeV Data for Tracks with  $P_T > 100$  MeV* , ATL-PHYS-INT-2010-112
- [97] D. de Florian, G. Ferrera, M. Grazzini and D. Tommasini, *Transverse-momentum resummation: Higgs boson production at the Tevatron and the LHC*, JHEP **1111** (2011) , arXiv:1109.2109 [hep-ph].
- [98] Statistical twiki, NuisanceCheck. <https://twiki.cern.ch/twiki/bin/view/AtlasProtected/NuisanceCheck>